



Rapid provision of maps and volcanological parameters: quantification of the 2021 Etna volcano lava flows through the integration of multiple remote sensing techniques

Cristina Proietti¹ · Emanuela De Beni¹ · Massimo Cantarero¹ · Tullio Ricci² · Gaetana Ganci¹

Received: 13 September 2022 / Accepted: 15 August 2023 / Published online: 13 September 2023
© The Author(s) 2023

Abstract

At active volcanoes recurring eruptive events, erosive processes and collapses modify the edifice morphology and impact monitoring and hazard mitigation. At Etna volcano (Italy) between February and October 2021, 57 paroxysmal events occurred from the South-East Crater (SEC), which is currently its most active summit crater. Strombolian activity and high lava fountains (up to 4 km) fed lava flows towards the east, south and south-west, and caused fallout of ballistics (greater than 1 m in diameter) within 1–2 km from the SEC. The impacted area does not include permanent infrastructure, but it is visited by thousands of tourists. Hence, we rapidly mapped each lava flow before deposits became covered by the next event, for hazard mitigation. The high frequency of the SEC paroxysms necessitated integration of data from three remote sensing platforms with different spatial resolutions. Satellite (Sentinel-2 MultiSpectral Instrument, PlanetScope, Skysat and Landsat-8 Operational Land Imager) and drone images (visible and thermal) were processed and integrated to extract digital surface models and orthomosaics. Thermal images acquired by a permanent network of cameras of the Istituto Nazionale di Geofisica e Vulcanologia were orthorectified using the latest available digital surface model. This multi-sensor analysis allowed compilation of a geodatabase reporting the main geometrical parameters for each lava flow. A posteriori analysis allowed quantification of bulk volumes for the lava flows and the SEC changes and of the dense rock equivalent volume of erupted magma. The analysis of drone-derived digital surface models enabled assessment of the ballistics' distribution. The developed methodology enabled rapidly and accurate characterisation of frequently occurring effusive events for near real-time risk assessment and hazard communication.

Keywords Multi-sensor · Remote sensing · Satellite images · Permanent camera images · UAS images · Rapid lava flow mapping · Etna volcano · GIS

This paper constitutes part of a topical collection: The lava fountain sequences in 2021 that disrupted the eruptive history of Mt Etna volcano, Italy.

Editorial responsibility: M. R. James

✉ Emanuela De Beni
emanuela.debeni@ingv.it

¹ Istituto Nazionale Geofisica e Vulcanologia, Sezione di Catania - Osservatorio Etneo, 95125 Catania, Italy

² Istituto Nazionale Geofisica e Vulcanologia, Sezione Roma 1, 00143 Roma, Italy

Introduction

Frequent eruptive events at an active volcano, coupled with erosive processes, instability episodes and subsequent structural failure, continuously modify the edifice morphology. These phenomena have major implications for the development of monitoring and hazard mitigation strategies (McGuire 1996). Near real-time monitoring and forecasting is a necessary step in mitigating the impact of an eruption and of lava flows. Sharing the produced maps with local civil protection in the first few hours following the start of an eruption helps to build effective mitigation strategies (Chevrel et al. 2022). Topographic changes at an active volcano necessitate updating topographic datasets, re-running lava flow emplacement models and quantification of volume variations (gains and losses) to support hazard assessment

and risk mitigation (Felpeto et al. 2007; Cappello et al. 2012; Turner et al. 2017; Neal et al. 2019; Chevrel et al. 2021; Barsotti et al. 2022; Pedersen et al. 2022). The topographic datasets that comprise digital surface models (DSMs) and orthophotos can be updated by processing data acquired by different sensors (thermal and visible cameras, and light detection and ranging, i.e. LIDAR) and platforms (satellites, aeroplanes, helicopters, unoccupied aerial systems, i.e. UASs, and from the ground). Satellite data, and in particular Pleiades optical data, have been previously processed to produce DSMs of volcanic areas and to quantify the eruptive deposits by comparing multi-temporal datasets (Pieri and Abrams 2004; Bagnardi et al. 2016; Ganci et al. 2018; Ganci et al. 2020; Pinel et al. 2020; Proietti et al. 2020; Gouhier et al. 2022; Ganci et al. 2022). In addition to satellite data that allow DSM extraction, satellite shortwave and thermal infrared images have been widely used for the monitoring of active volcanoes since the 1960s, providing repeated low-cost and synoptic observations with a known revisit time (e.g. Francis 1979; Francis and Rothery 1987; Oppenheimer et al. 1993; Wooster and Rothery 1997; Lachlan-Cope et al. 2001; Patrick et al. 2005; Gray et al. 2019; Ganci et al. 2020). Thermal data can be provided at low-spatial (1 to 4 km) but high-temporal (30 min to 3 day) resolution by the advanced very-high-resolution radiometer, the along-track scanning radiometer and the geostationary operational environmental satellite or at high-spatial (30 to 120 m) but low-temporal resolution (16 days) by the Landsat 7 enhanced thematic mapper plus (Harris et al. 1997, 1999, 2000 and 2001). Data from aerial vehicles have been traditionally used for volcanological monitoring and mapping, also applying the structure from motion processing method (Baldi et al. 2000; Harris et al. 2007; Marsella et al. 2009; Marsella et al. 2014; De Beni et al. 2015; Dvigalo et al. 2016; Neri et al. 2017; Thiele et al. 2017). UASs have been used extensively to derive topographic data for mapping volcanic areas, supporting lava hazard analyses, estimating lava flow and dome volumes and performing high-resolution morphometric analysis (e.g. Turner et al. 2017; Dietterich et al. 2017; Favalli et al. 2018; De Beni et al. 2019; Wakeford et al. 2019; James et al. 2020; Lormand et al. 2020; Andaru et al. 2021; Civico et al. 2021; Carr et al. 2022; Civico et al. 2022; Román et al. 2022). LIDAR data have been acquired on active volcanoes for measuring lava flows and domes as well as crater rim changes (e.g. Favalli et al. 2009; Marsella et al. 2009; Jozkow et al. 2016; Alsadik and Remondino 2020; Dietterich et al. 2021; Gomez et al. 2022). Satellite data allow production of DSMs from sub-metre (WorldView and Pleiades) to metre (Ikonos and Quickbird) sampling distances, relatively high temporal frequency (hours to days, if using multiple platforms), metre-level accuracy and swath width up to two tens of kilometres (Proietti et al. 2020). Surveys with aircraft, helicopters and UAS can be used instead of, or

in addition to, satellite data as they can provide very high-resolution (cm-pixel) data for mapping and DSM generation (Turner et al. 2017). The advantages of UAS surveys over other remote sensing techniques are as follows: (1) low cost of survey; (2) low-altitude flight operations that result in a centimetre-scale spatial data; (3) automated mission planning that allows acquisition of consistent and repeat datasets for the same area; and (4) increased safety for the pilot compared to in situ measurements (Turner et al. 2017). Moreover, remotely piloted systems represent a platform capable of delivering rapid, reactive and repeatable data acquisition for any location and benefit from a high degree of flexibility in terms of flight planning (Turner et al. 2017).

Advanced remote observation methods now play an important role in the understanding, tracking and monitoring of volcanic processes for both remote volcanoes where field surveys are challenging and for well-monitored sites (Pyle et al. 2013). Volcanic activity generally affects large areas (for example on Etna between 0.03 and 40 km², Coltelli et al. 2017; Branca et al. 2013), and may develop rapidly (seconds to hours). Therefore, it is desirable to integrate data acquired by different in-orbit and airborne remote sensing platforms that have different spatial and temporal resolutions, and images acquired by ground-based sensors (Honda and Nagai 2002; Torres et al. 2004; James et al. 2006, 2007, 2012 and 2014; Ernst et al. 2008; Diefenbach et al. 2012; Ganci et al. 2013 and 2020; Coltelli et al. 2017; Carr et al. 2019; Di Traglia et al. 2020; Calvari et al. 2021; Caballero et al. 2022; Musacchio et al. 2023). However, critical gaps in the data acquisition capabilities within each of all remote platforms persist due to the rapid, unpredictable and dangerous nature of many volcanic processes, and poor meteorological conditions. For these reasons, a multi-sensor and multi-platform approach is valuable when there is a need to collect data with rapid recurrence, such as to map multiple eruptions over 24 h. On Etna, such behaviour has been well documented since the 1970s, particularly since 2011 and into 2021 (e.g. Tanguy and Patané 1984; Chester et al. 1985; Behncke et al. 2006; Behncke et al. 2014; De Beni et al. 2015; Ganci et al. 2019; Proietti et al. 2020; Ganci et al. 2022).

Here, we focus on Etna's 2021 eruptive activity which, due to the short intervals between events, required rapid mapping and quantification of each lava flow field (before deposits became covered by the next event), evaluation of the SEC cone growth and estimates of proximal and distal fallout deposit volumes. Our analysis is based on combining data with a range of spatial and temporal resolutions from different multiple remote sensing techniques and platforms (satellite, ground and UAS).

Etna's summit activity

Etna is a composite basaltic stratovolcano, located along the Ionian coast of eastern Sicily (Italy), and characterised by

quasi-persistent activity at its four summit craters: Voragine (VOR), North-East Crater (NEC), Bocca Nuova (BN) and South-East Crater (SEC, Fig. 1). The summit craters gave rise to gas emissions, Strombolian to lava fountain activity, and lava overflows. Paroxysms are among the most powerful explosive events to occur at Etna's summit craters (Bombrun et al. 2016; Corsaro et al. 2017). They typically last no longer than a few hours (Barsotti et al. 2010) and are associated with violent Strombolian activity or pulsating to sustained lava fountains, and produce eruptive columns of ash, lapilli and steam, rising up to 14 km above sea level (Corsaro et al. 2017). In most cases, these events also produce fast-moving lava flows that extend a few kilometres from the summit and may continue after the end of the explosive phase (e.g. Alparone et al. 2003; Behncke 2009; Behncke et al. 2014; De Beni et al. 2015; Ganci et al. 2018; Proietti et al. 2020; Corsaro and Miraglia 2022). Summit lava flows are not life-threatening due to their slow propagation, but danger can result from associated phenomena, e.g. the interaction between lava flow and snow or water to create localised phreatic explosions (Chester et al. 1985; Blong 1984). Lava fountains and sustained Strombolian activity produce fallout of ballistic juvenile and lithic bombs in areas less than 5 km from the vent. This fallout represents a danger to tourists visiting the summit of the volcano and sportspeople (both in winter for skiing and in the other seasons for

trekking), as well as guides and researchers (Andronico et al. 2015 and 2021; Osman et al. 2019).

Plumes produced during paroxysms are commonly dispersed by the prevailing westerly winds to deposit tephra over the eastern flanks of the volcano. Lapilli-sized particles and even blocks and bombs can be transported downwind up to several kilometres, while ash-sized particles may be transported over hundreds of kilometres. In a few of Etna's paroxysms, for example on 23 November 2013, ash and tephra fallout was observed up to Calabria and Puglia regions in southern Italy, and as far as 400 km from the volcano (Andronico et al. 2015; Donnadiu et al. 2016). Small-volume pyroclastic density currents (PDCs, $< 2 \times 10^6 \text{ m}^3$) may also be produced during or after a paroxysm. PDCs not directly associated with the fountain can be due to (1) collapse of pyroclastic fountains; (2) the failure and/or sliding of pyroclastic deposits emplaced on steep slopes during intense lava fountaining; (3) the gravitational collapse of lava flow fronts; (4) the lava interaction/mixing with wet rocks or snow (Behncke 2009; Norini et al. 2009; Andronico et al. 2018).

Approximately 30 paroxysmal events occurred at Etna's summit craters between 1900 and 1970. More than 180 summit paroxysms have occurred since the 1970s, suggesting they are occurring at an increased frequency (Behncke and Neri 2003). A particularly high number of events (66) were observed between January and August 2000, and most of them occurred at the SEC (Alparone et al. 2003; Behncke et al. 2006). NEC generated its last paroxysms in 1995–1996 and 1998, and BN in 1999 (Allard et al. 2006; Behncke et al. 2003). A lower number of paroxysms have occurred at VOR, but these are more violent and briefer than those at the SEC, NEC and BN. The VOR paroxysms of 22 July 1998 and 4 September 1999 were among Etna's most powerful eruptive events of the past century (Corsaro et al. 2017). The first event generated a sub-Plinian eruption column that ascended 10 km, resulting in widespread ash fall, mainly to the south (Aloisi et al. 2002). The latter event formed a 5-cm-thick tephra layer in Giarre, ~10 km from the vent, but it was not well documented (Andronico et al. 2015).

Etna's explosive activity 2010–2020

In 2010, Etna exhibited mild degassing activity, followed in 2011 by Strombolian activity from both the BN and the SEC. Between 2011 and 2013, discontinuous and vigorous Strombolian activity at the BN built a small cone on the crater floor and fed a new lava flow (Proietti et al. 2020). At the VOR, two brief periods of eruptive activity in early 2013 and early 2015 consisted of moderate Strombolian explosions and ash emissions (Corsaro et al. 2017). In May 2016, seven paroxysmal

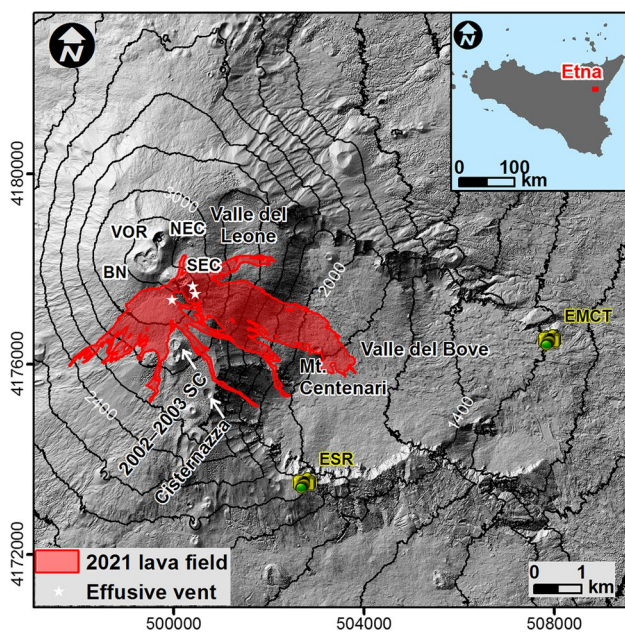


Fig. 1 Composite lava flow field from all the eruptive events of 2021, superimposed on shaded relief extracted from a Pleiades triplet of 22 August 2020; contour lines are shown every 200 m, elevation is ellipsoidal. The figure also shows the summit craters, the two thermal cameras (EMCT and ESR), and the location of effusive vents (white stars which are not to scale). The inset shows the location of Etna with respect to Sicily. SC stands for scoria cones

events at VOR formed ash plumes up to 14 km high. The related deposits filled the crater and the adjoining BN and overflowed on the western flank from BN lower rim (Proietti et al. 2020). Between September 2019 and mid-May 2020, discontinuous Strombolian and effusive activity on the VOR crater floor caused the growth of an intra-crater cone, and fed lava flows from VOR into BN. Between December 2020 and April 2021, explosive activity occurred again at the VOR, and was associated with sporadic lava effusion (Pioli et al. 2022).

At the SEC, fifty paroxysms occurred between 2011 and 2014 and dramatically changed its morphology with the formation of a new scoria cone, initially called New South-East Crater (NSEC). The overlapping of all the lava flows, emplaced during each paroxysm, produced composite lava flow fields along the east, south and west flanks. After 2013, the eruptive activity led to the coalescence of the NSEC with the SEC (Vicari et al. 2011; Andronico et al. 2014; Behncke et al. 2014; De Beni et al. 2015; Falsaperla and Neri 2015; Acocella et al. 2016; Andronico et al. 2018; Proietti et al. 2020). Between 2017 and 2020, discontinuous vigorous Strombolian and effusive activity occurred at the SEC. In 2020, four paroxysmal events at the SEC produced lava flows that extended 2.8 km to the SE, into the Valle del Bove, and to the SW as well as 1.6 km to the NE, into the Valle del Leone (De Beni et al. 2021; Calvari and Nunnari 2022). This activity culminated in the SEC explosive-effusive events of 2021.

The 2021 SEC activity

In 2021, the SEC gave rise to 58 paroxysmal events in just over 9 months, from 18 January to 23 October 2021. These events fed lava flows that rapidly propagated to the S-SW and into the Valle del Bove and the Valle del Leone, formed eruptive columns up to 11 km in height and caused fall-out of ballistics greater than 1 m in diameter within 1–2 km from the SEC, and moderate to light tephra fallout at increasing distances from the proximal to distal areas. The proximal area is that including the original volcanic landform (i.e. the source vent and the SEC cone) and the ‘distal area’ represents the area covered by a fallout deposit that continuously mantles the topography (Nèmeth and Martin 2007). The first lava fountain occurred on 18 January and was preceded, on 17 and 20 January, by effusive activity at the SEC that fed lava flows towards the Valle del Bove (Andronico et al. 2021; Marchese et al. 2021; Calvari and Nunnari 2022). About a month later, a series of paroxysmal events began at the SEC, with 17 lava fountains occurring between 16 February and 1 April 2021, each lasting between 0.8 and 10.5 h, with an average duration of 2.9 h. The time interval between two successive events ranged from just over 1 day to just under 8 days (Table 1). On 19 May 2021, paroxysms resumed after a month and a half of quiescence. Until 23 October, the SEC produced 40 paroxysms that lasted between 0.5 and 4.9 h, with an average duration of 1.6 h. The

Table 1 Progressive number of the paroxysmal event (PE) of the first cycle; event date (day and month, the year is 2021 for all events); start time of lava flow (LFI); start, end time and duration of lava fountain (LFo); time interval between two lava fountains (LFos); dates are shown, along with start and end times for events that occurred on two or more days; – denotes missing information

PE number	Date	LFI start time (date)	LFo start time (date)	LFo end time (date)	LFo duration (h)	Interval between two LFos (d)
1	16 February	15:59	16:10	17:00	0.8	
2	17–18 February	22:30 (17-02)	23:56 (17-02)	00:55 (18-02)	1.0	1.3
3	19 February	07:55	08:46	10:00	1.3	1.3
4	20–21 February	21:30 (20-02)	22:00 (20-02)	01:20 (21-02)	3.3	1.5
5	22–23 February	22:23 (22-02)	22:27 (22-02)	00:10 (23-02)	1.7	1.9
6	24 February	19:22	19:00	21:20	2.3	1.6
7	28 February	7:39	07:39	08:33	0.9	3.5
8	02 March	–	12:24	14:50	2.4	2.2
9	04 March	03:05	07:50	09:20	1.5	1.7
10	07 March	03:50	06:16	07:10	0.9	2.9
11	09–10 March	19:13 (09-03)	00:47 (10-03)	03:30 (10-03)	2.7	2.7
12	12 March	06:54	07:30	09:55	2.4	2.2
13	14–15 March	00:05 (15-03)	23:44 (14-03)	02:42 (15-03)	3.0	1.6
14	17 March	02:25	02:17	06:17	4.0	2.0
15	19 March	–	08:30	10:31	2.0	2.1
16	23–24 March	02:35 (24-03)	22:16 (23-03)	08:45(24-03)	10.5	4.5
17	31 March–01 April	09:00 (31-03, effusive vent)	22:57 (31-03)	08:00 (01-04)	9.0	7.7

time interval between successive events ranged from about 4 h to 32 days (Table 2). Based on the timing of the 2021 events, we can divide them into two eruptive cycles: the first from 16 February to 1 April, and the second from 19 May

to 23 October. During both cycles, fountaining was generally preceded by Strombolian activity and accompanied by lava flows, mostly towards the Valle del Bove and SW that formed composite lava fields (Fig. 1 and Fig. 2). During

Table 2 Progressive number of the paroxysmal event (PE) of the second cycle; event date (day and month, the year is 2021 for all events); start time of lava flow (LFI); start, end time and duration of

lava fountain (LFo); time interval between two lava fountains (LFos); dates were shown along with start and end times only for events that occurred on two or more days; – denotes missing information

PE number	Date	LFI start time	LFo start time	LFo end time	LFo duration (h)	Interval between two LFos (d)
18	19 May	02:30	01:15	05:12	4.0	45.7
19	21 May	–	01:04	02:54	1.8	2.8
20	22 May	21:02	20:39	22:38	2.0	0.7
21	24 May	–	20:25	22:06	1.7	1.9
22	25 May	18:44	18:21	19:36	1.2	0.8
23	26 May	–	01:55	03:47	1.9	0.3
24	26 May	11:07	10:35	11:30	1.0	0.3
25	27 May	Sustained Strombolian activity, no LFo				
26	28 May	07:06	06:47	07:25	0.6	0.5
27	28 May	–	15:40	16:15	0.5	0.4
28	28 May	–	20:07	20:50	0.7	0.1
29	30 May	–	04:40	05:45	1.0	1.3
30	02 June	–	08:30	10:45	2.2	3.1
31	04 June	16:04	16:20	17:30	1.2	2.2
32	12 June	13:48	19:30	23:15	3.7	8.1
33	14 June	21:32	21:46	22:44	1.0	1.9
34	16 June	11:47	11:47	12:50	1.0	1.5
35	17–18 June	20:20 (17-06)	23:20 (17-06)	00:10 (18-06)	0.8	1.4
36	19 June	18:30	19:00	20:18	1.3	1.8
37	20–21 June	22:15 (20-06)	22:15 (20-06)	00:12 (21-06)	1.9	1.1
38	22 June	02:55	02:55	04:12	1.3	1.1
39	23 June	02:13	02:44	03:17	0.5	1.0
Effusive Event (EE)	23–26 June	04:25 (23-06)	No LFo	No LFo	No LFo	No LFo
40	23 June	18:28	18:00	19:00	1.0	0.6
41	24 June	09:55	09:55	10:42	0.8	0.6
42	25 June	01:15	01:00	01:48	0.8	0.6
43	25 June	18:25	18:26	19:15	0.8	0.7
44	26 June	15:47	15:47	17:00	1.2	0.9
45	27 June	08:25	09:00	09:48	0.8	0.7
46	28 June	before 15:01	14:58	15:30	0.5	1.2
47	01–02 July	23:37 (01-07)	22:50	00:50 (02-07)	2.0	3.3
48	04 July	15:25	15:25	17:00	1.6	3.6
49	06–07 July	–	22:30 (06-07)	00:19 (07-07)	1.8	2.4
50	08 July	20:45	20:45	22:47	2.0	2.8
51	14 July	10:40	11:01	12:30	1.5	5.5
52	20 July	05:47	05:47	08:48	3.0	5.8
53	31 July	19:15	21:21	23:30	1.9	11.5
54	08–09 August	23:10 (08-08)	00:40 (09-08)	04:00 (09-08)	3.3	8.0
55	29 August	18:19	15:45	20:37	4.9	20.5
56	21 September	07:55	07:55	09:27	1.5	22.5
57	23 October	09:00	08:42	10:20	1.6	32.0

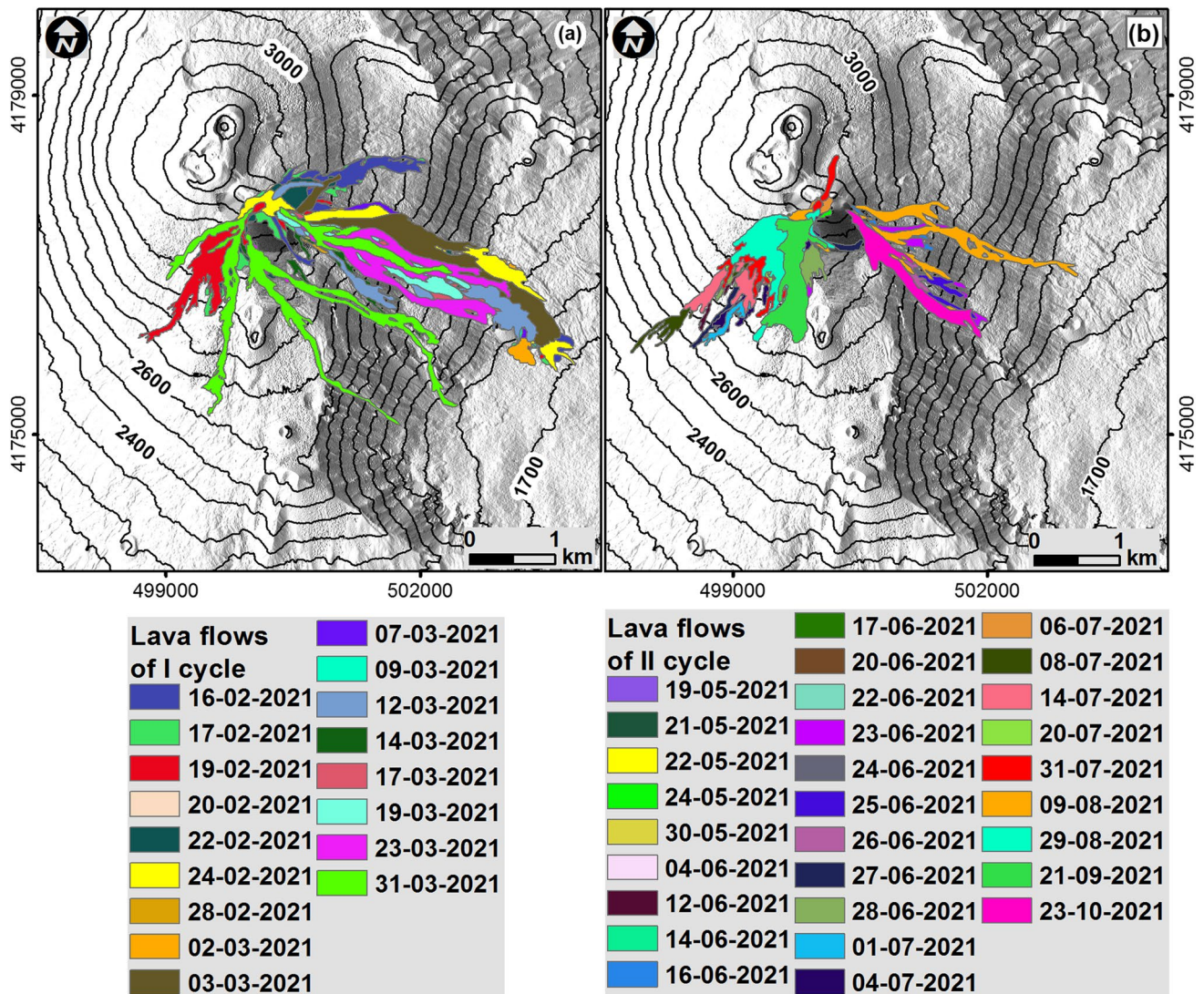


Fig. 2 **a** Lava flows of the first eruptive cycle; **b** lava flows of the second eruptive cycle. In both figures the background image is the Pleiades shaded relief of 22 August 2020; contour lines are shown

every 100 m, elevation is ellipsoidal. Each legend relates to the figure immediately above it

three events, effusive vents opened at the SEC base (Fig. 1, between 3000 and 3100 m a.s.l.): to the south, 31 March–1 April, and to the south-east, as on 23–26 June and on 09 August. These vents fed lava flows that mainly advanced towards the Valle del Bove, whereas smaller flows extended to the S and SW. Five events were also accompanied by short pyroclastic flows propagating into the Valle del Bove. Those of 16 February resulted from a partial cone collapse. Those of 28 February, 24 March and 23 October resulted from the failure of pyroclastic fall deposits emplaced on a steep slope (with flows on 23 October travelling towards the S and SE). These events are described in the weekly ‘Bollettino Etna’ activity reports (<https://www.ct.ingv.it/index.php/monitraggio-e-sorveglianza/prodotti-del-monitoraggio/bollettini-settimanali-multidisciplinari?filter%5Bsearch%5D=Etna>).

Material and methods

Data and pre-processing

To analyse the 2021 Etna paroxysmal events, we analysed images obtained from multiple remote sensing techniques and platforms in ESRI ArcGIS software (<https://www.esri.com/en-us/arcgis/about-arcgis/overview><https://www.esri.com/en-us/arcgis/about-arcgis/overview>, v10.6). Satellite images were acquired from Sentinel-2 MultiSpectral Instrument (MSI), PlanetScope, Skysat, Landsat-8 Operational Land Imager (OLI) and Pleiades, depending on data availability and weather conditions (mostly cloud cover). In addition, UAS-borne thermal and visible cameras provided higher-spatial resolution (cm-scale) images.

Lastly, images acquired by the INGV-OE permanent network of surveillance cameras were orthorectified and analysed.

To produce a DSM of Etna that quantifies the pre-paroxysm topography with a spatial resolution of 1 m and a vertical accuracy of 1 m, we processed a triplet of Pleiades satellite visible images acquired on 22 August 2020 (image spatial resolution of 0.5 m, acquired on demand) using the MicMac open-source library (Rupnik et al. 2017). DSM accuracy was evaluated by measuring the standard deviation of the difference between the 2020 DSM and a 2015 Pleiades DSM in areas where no topographic changes occurred (Ganci et al. 2019).

We analysed orthorectified images acquired by Skysat and PlanetScope (spatial resolution of 0.5 and 3.7 m, respectively; acquired on demand and every day, respectively) by setting thresholds on the near-infrared and red ($\sim 0.8 \mu\text{m}$ and $\sim 0.6 \mu\text{m}$, respectively) bands (Ganci et al. 2019).

Active or recently erupted lava flows were identified in orthorectified images acquired by Sentinel-2 MSI (spatial resolution of 10 m and 20 m, for visible and thermal images respectively; temporal resolution of 2–3 days) and Landsat 8 OLI sensors (spatial resolution of 30 m; temporal resolution of 7–9 days). The flows were identified by thresholding in the short-wave infrared (SWIR) bands (Bands 7 and 12 for Landsat 8 and Sentinel-2, respectively) centred at $\sim 2 \mu\text{m}$ (Ganci et al. 2018; Cappello et al. 2019).

If satellite or UAS images were not available or adequate for satisfactory mapping, we used images acquired by Monte Cagliato and Schiena dell'Asino thermal cameras (EMCT and ESR, frame rate of 2 frame/s; Fig. 1). These two sensors belong to a permanent network of ground-based surveillance cameras (visible and thermal) that is installed on Etna's flanks and is managed by the Istituto Nazionale di Geofisica e Vulcanologia-Osservatorio Etneo (INGV-OE <https://www.ct.ingv.it/index.php/monitoraggio-e-sorveglianza/segnali-in-tempo-reale/video-sorveglianza-vulcanica-etna>). At the end

of the paroxysms, we selected the images that effectively showed the lava fields. We orthorectified these images by re-projecting them onto the 2020 DSM using an algorithm that considers the position and orientation of each camera (Ganci et al. 2013; Calvari et al. 2021), to obtain georeferenced thermal images (spatial resolution of 5 m). For image orthorectification, it is of primary importance to use an up-to-date DSM of the volcano since morphological changes will increase error in the image georeferencing and orthorectification (Ganci et al. 2013).

In 2021, we carried out nine UAS surveys with the aim of monitoring eruptive activity and acquiring data useful for photogrammetry processing (Table 3). Six surveys were performed over the SEC crater, using a DJI Mavic Enterprise. The high-resolution visible (12 Mpx) and thermal images ($160 \times 120 \text{ px}$) collected enabled monitoring the morpho-structural evolution of the SEC summit portion, which was deeply fractured and potentially unstable. Two surveys were performed over the Valle del Bove, where most of the lava flows were emplaced, using a DJI Mavic Enterprise and a DJI Mavic 2 Pro to collect visible images (20 Mpx). One UAS survey was performed in the area of Cisternazza, a pit crater that formed during the 1792 eruption (Fig. 1), using a DJI Phantom 4 Pro to collect high-resolution visible images (20 Mpx). A previous survey in the Cisternazza area had been carried out in 2020 using the same UAS (Table 3).

The UAS surveys only partially covered the areas to be monitored; images collected above the Valle del Bove covered only a part of the 2021 lava flows, and the SEC surveys generally covered only its south and east sides. These partial coverages reflect the difficulty of UAS surveying in hostile environments such as the summit area of Etna and the Valle del Bove. Due to the need to operate from a safe location, it was only possible for the UAS to take off from the 2002–2003 scoria cone (Fig. 1). From this take-off point, the north side of the SEC is not visible and UAS

Table 3 Summary table of the UAS surveys; UAS model; survey target and goal indicate the area of interest and the focus of the overflight; the resolution of the derived DSMs and orthomosaics are given

Survey date	UAS	Survey target	Goal	Covered area (km ²)	Number of images	DSM resolution (cm/px)	Orthomosaic resolution (cm/px)
05 August 2020	DJI Phantom 4 pro	Cisternazza	Photogrammetry	0.13	1082	7.6	1.9
03 March 2021	DJI Mavic Enterprise	SEC	Photogrammetry and Monitoring	1.07	60	55.0	14.0
12 March 2021	DJI Mavic Enterprise	VdB	Monitoring	–	174	–	–
27 March 2021	DJI Mavic 2 pro	VdB	Photogrammetry and Monitoring	15.8	277	48.9	12.2
29 March 2021	DJI Mavic Enterprise	SEC	Monitoring	–	544	–	–
16 Sept. 2021	DJI Phantom 4 pro	Cisternazza	Photogrammetry	0.13	974	4.5	2.3
16 Sept. 2021	DJI Phantom 4 pro	SEC	Photogrammetry and Monitoring	1.3	356	44.0	11.0
30 Sept. 2021	DJI Mavic Enterprise	SEC	Monitoring	–	70	–	–
04 Oct. 2021	DJI Mavic Enterprise	SEC	Monitoring	–	544	–	–
20 Oct. 2021	DJI Mavic Enterprise	SEC	Monitoring	–	584	–	–

flight regulations did not allow operation beyond visual line of sight. Not all flyovers yielded useful images for photogrammetric analysis due to the presence of gas and clouds that obscured the ground. Suitable visible images (Table 3) were processed through a structure-from-motion photogrammetric software (Agisoft Metashape v1.6.6, <https://www.agisoft.com>.) and we extracted DSMs and orthomosaics with resolutions between 4 and 55 cm/px. During data processing, the SEC and the Valle del Bove datasets were georeferenced using only the aircraft position measured by the on-board GNSS. This is because we were unable to position the ground control points (GCPs) around the SEC cone and inside the Valle del Bove due to volcanic hazard and the extremely rough terrain. In contrast, we georeferenced and processed the data acquired on the Cisternazza area using 6 GCPs, whose positions were measured through a Glonass GNSS with centimetric to sub-centimetric precision. We performed real-time correction of the GNSS data using a reference station of the INGV permanent GNSS network (RING <http://ring.gm.ingv.it/>). Before analysing the elevation changes of the SEC and the Valle del Bove, we co-registered the different pairs of point clouds by manual and automatic alignment through the Cloud Compare (v2.12.4) open-source software (<https://www.danielgm.net/cc/><https://www.danielgm.net/cc/>). In this way, we improved the correspondence between two datasets acquired at different dates (pre and post-eruption). We then exported the point clouds

into DSMs through the Global Mapper software (v22.0, <https://www.blumarblegeo.com/global-mapper/>) and managed the DSMs with the ESRI ArcGIS software.

Rapid lava flow mapping

We rapidly mapped almost all the lava flows in ESRI ArcGIS software. For seven events (PEs from 22 to 24, from 26 to 28, and 36 in Table 2), we did not have satellite, UAS or surveillance camera images available owing to poor weather conditions. Therefore, we did not map the corresponding lava flows. In three more cases, we had only one reference dataset for two paroxysmal events that were very close in time (PEs 30 and 31; PEs 42 and 43; PEs 44 and 45 in Table 2). Because we were unable to distinguish and separately map the individual lava flows, we produced three maps, each covering the cumulative deposits from two paroxysms. For each mapped lava flow, we measured geometrical parameters of maximum length, minimum front elevation and covered area. We recorded these measurements into a geodatabase GIS along with the analysed datasets (Tables 4 and 5), the start time of lava fountains (LFo) and lava flows (LFI), as well as the end time of lava fountains (Tables 1 and 2). These times are determined by INGV-OE control room staff from surveillance camera images, and are reported in the “Bollettino Etna” activity reports. The end of both lava effusion and of the front advance is not exactly identifiable from image analysis due to the gradual

Table 4 Progressive number of the paroxysmal event (PE) of the first cycle; datasets analysed for mapping the lava flows (acquisition date: day and month, the year is 2021 for all datasets); directions, maxi-

imum length (Max L) and minimum (Min) front elevation (ellipsoidal values) of the lava flows (LFIs)

PE number	Analysed datasets (date)	LFI directions	Max L (km)	Min front elevation (m)
1	Skysat and Aster (17-02)	E, NE	4.0	1735
2	Skysat (18-02)	SW, E, NE	4.1	1740
3	Skysat (20-02)	SW, E	3.8	1740
4	Sentinel 2 (21-02)	E, SW	3.4	1870
5	Sentinel 2 (23-02)	SW, E, NE	3.0	1950
6	Sentinel 2 and Planescope (26-02)	SW, E	4.3	1700
7	Sentinel 2 (28-02)	SW, E	2.5	2050
8	Sentinel 2 (10-03), Planescope (06-03)	E	3.5	1760
9	Sentinel 2 (10-03), Planescope (06-03)	SW, E, NE	3.5	1780
10	EMCT (07-03)	E	3.3	1790
11	Planescope (11-03), UAS images (12-03)	E	3.3	1770
12	Sentinel 2 (13-03), Planescope (16-03), UAS images (12-03)	E,NE	3.2	1790
13	Planescope (16-03-2021), EMCT (14-03)	E, SE	2.7	1950
14	EMCT (17-03)	E	2.8	1930
15	Planescope (24-03), EMCT (19-03)	E	2.4	2020
16	Sentinel 2 (25-03), EMCT (23-03), UAS images (27-03)	E, SE	2.5	1920
17	Sentinel 2 (04-04), Planescope (01-04), ESR (02-04)	E,SE, SW	3.5	1820

Table 5 Progressive number of the paroxysmal event (PE) of the second cycle; datasets analysed for mapping the lava flows (acquisition date: day and month, the year is 2021 for all datasets); directions, maximum length (Max L) and minimum (Min) front elevation (ellip-

soidal values) of the lava flows (LFIs); *, ** and *** dataset of cumulative maps, each referring to two paroxysms very close in time; # not mapped lava flow owing to poor wheatear; – missing information

PE number	Analysed dataset (date)	LFI directions	Max L (km)	Min front elevation (m)
18	Sentinel 2 and PlanetScope (19-05)	SW	1,8	2810
19	Sentinel 2 (22-05)	SW	1.0	3030
20	Sentinel 2 (24-05)	SW	0.5	3090
21	Landsat 8 (24-05)	SW	0.9	3040
22	–, #	SW	–	–
23	–, #	SW	–	–
24	–, #	SW	–	–
25	–	No lava flow	No lava flow	No lava flow
26	–, #	SW	–	–
27	–, #	SW	–	–
28	–, #	–	–	–
29	Sentinel 2 (01-06)	SW	0.9	3020
30	Sentinel 2 (08-06)*	SW	0.9	3020
31	Sentinel 2 (08-06)*	SW	0.9	3020
32	Sentinel 2 (13-06), Skysat (15-06)	SW, SE	2.2	2670
33	Sentinel 2 (16-06), Skysat (15-06)	SW, SSE	1.2	3020
34	Landsat 8 (17-06), Skysat (17-06)	SW-S, E	1.3	2690
35	Sentinel 2 and Skysat (18-06)	SW-S	0.8	3050
36	–, #	SW	–	–
37	Sentinel 2 (21-06)	S	1.3	2900
38	Sentinel 2 (23-06)	S	1.3	2910
39	Sentinel 2 (23-06)	SW	1.1	2980
EE	Sentinel 2 (26-06 and 28-06), EMCT (24-06, 25-06 and 26-06)	E	2.0	2200
40	Sentinel 2 (26-06)	SW	1.3	2900
41	Sentinel 2 (26-06)	SW	1.2	2960
42	Sentinel 2 (26-06), EMCT (25-06)**	SW-S, E	0.8	3040
43	Sentinel 2 (26-06), EMCT (25-06)**	SW-S, E	0.8	3040
44	Sentinel 2 (28-06) and EMCT (26-06)***	SW	2.4	2590
45	Sentinel 2 (28-06)***	SW-SE	2.4	2590
46	Sentinel 2 (03-07)	SW-S	1.5	2780
47	Sentinel 2 (03-07 and 06-07)	SW	2.0	2650
48	Sentinel 2 (06-07) and PlanetScope (05-07)	SW	1.9	2700
49	Sentinel 2 (08-07)	SW	1.6	2900
50	Sentinel 2 (08 and 11-07)	SW	2.9	2350
51	Sentinel 2 (16-07)	SW	2.1	2700
52	Sentinel 2 (26-07)	SW	1.6	2890
53	Sentinel 2 (02-08)	SW, N	1.7	2840
54	Sentinel 2 (10 and 12-08-2021), EMCT (10-08)	SW, E	2.8	1950
55	Sentinel 2 (30-08)	SW, E	1.8	2700
56	Sentinel 2 (21-09)	SW	1.5	2840
57	Sentinel 2 (25-10), EMCT (23-10), ESR (23-10)	E	2.2	2180

nature of the cooling process. After the emplacement of each lava flow, an initial bulk volume estimate was recorded in the geodatabase, based on a planimetric approach, i.e.

multiplying the measured area by a plausible average thickness of 2 m, estimated from ground surveys (Stevens et al. 1999).

We overlaid all the mapped lava flows to produce a 2021 resurfacing map for Etna (Proietti et al. 2011), which indicates how many times each cell (of the 2020 DSM) was covered by lava in 2021. We also sequentially superimposed the map of each lava flow, starting from that of 16 February, to follow the temporal evolution of the 2021 resurfacing map.

A posteriori cross-section analysis of the lava flows

Because high-resolution DSMs were not available for each event, we performed (in ESRI ArcGIS) an a posteriori analyses to evaluate the bulk volume of each of the 2021 lava flows by applying the cross-section approach (De Beni et al. 2021). This method is based on two assumptions: (1) the thickness of a simple lava field remains constant on a surface with a constant slope; (2) comparable average thicknesses are associated with comparable slopes. Each of the 2021 eruptive events lasted from a few hours to less than 3 days, thus formed simple lava flows (*sensu* Walker 1971, 1973) whose emplacement and thickening are essentially governed by slope changes. We evaluated the slope from the 2020 DSM and defined seven polygons that envelope areas with homogeneous slope values (Fig. 3a). Then we used these polygons to cut each simple lava flow into parts. We drew eleven cross-sections along the lava flows emplaced on 23 and 31 March 2021 in Valle del Bove and towards S-SE, respectively (Fig. 3a and b). The cross-sections were located in two slope areas (0–25° and 26–34°) and were plotted where the flow morphology and their thicknesses are unambiguously measurable on the 27 March and the 16 September 2021 DSMs, respectively. The first DSM was acquired towards the end of the first eruptive cycle, shortly after the emplacement of the 23 March lava field. The S-SE branch of the March 31 lava flow was not covered by successive events, so it could be measured on the latter DSM. Interpolation of the pre-eruption surface at the eleven cross-sections allowed us to estimate the average thickness to be assigned in each slope area and to the flow portions inside them (Fig. 3c–g). We calculated the bulk volume of each flow through the planimetric approach (Stevens et al. 1999). We estimate an error of 20% (Table 6) for these volumes, which is the magnitude commonly associated with this approach (Calvari et al. 1994). For each lava flow that we did not map (owing to poor weather, # in Table 5), we assigned a volume equal to that measured for an event with the same flow direction and lava fountain duration. For each pair of paroxysms very close in time with only one reference dataset (*, **, *** in Table 5), a total volume (V_{tot}) was calculated by multiplying the measured area (which is cumulative for both events) by doubling the average single-flow thickness, as evaluated from the cross-section analysis (described above). This

approach might overestimate lava volume, but we assume to less than the estimated error of 20% (Table 6). The total volume was then distributed between the two events (1 and 2) proportionally to their durations (D_1 and D_2), e.g.:

$$V_1 = V_{tot} * \frac{D_1}{D_1 + D_2}$$

A posteriori topographic analysis of the lava flows

We also estimated bulk lava flow volumes through a posteriori analysis of the available DSMs in ESRI ArcGIS. We applied the topographic approach that calculates the elevation differences between datasets acquired on different dates before, during or after an eruption (Stevens et al. 1999). In particular, we compared the 27 March 2021 DSM and the 2014 Etna's DSM (pixel size of 1.5 m, De Beni et al. 2015) in the Valle del Bove. The 2014 DSM is less up-to-date than the 2020 one; however, after its acquisition, only one lava flow was emplaced on the analysed zone (06–08 December 2015, Proietti et al. 2020). We preferred to use this reference surface because, inside the Valle del Bove, it is more accurate and less noisy than the 2020 one and therefore it allows for a better estimation of the lava flow thicknesses. The topographic comparison of the two DSMs allowed measuring the thickness accumulated during the paroxysmal events from 1 to 16 (Fig. 4a and Table 1). The measured value was divided by the number of overlapped lava flows (Fig. 4b) to evaluate an average thickness of 2.0 m for each flow unit. This value is congruent with the average thickness estimated by ground observation and measurements, which were used for the preliminary volume evaluation. It is also congruent with the average thicknesses assigned to slope areas D and E based on the cross-section analysis (Fig. 3g). We analysed a cross-section cutting the Monti Centenari scoria cone (formed during the 1852 eruption), we identified the overlap area of the different lava flows and we distinguished the different contributions to lava thickness (Fig. 3e). By comparing the 2021 and 2014 DSMs, we also measured the lava thickness accumulated within the Monti Centenari scoria cone (formed during the 1852 eruption) during the 9 and 12 March 2021 events (Fig. 3f).

A posteriori topographic analysis of the SEC cone

We measured the bulk volume changes of the SEC cone and its elevation through topographic comparison (Stevens et al. 1999) in ESRI ArcGIS, of the 16 September 2021 and the August 2020 DSMs. In this case, we preferred the 2020 DSM over that from 2014, because it better represents the pre-2021

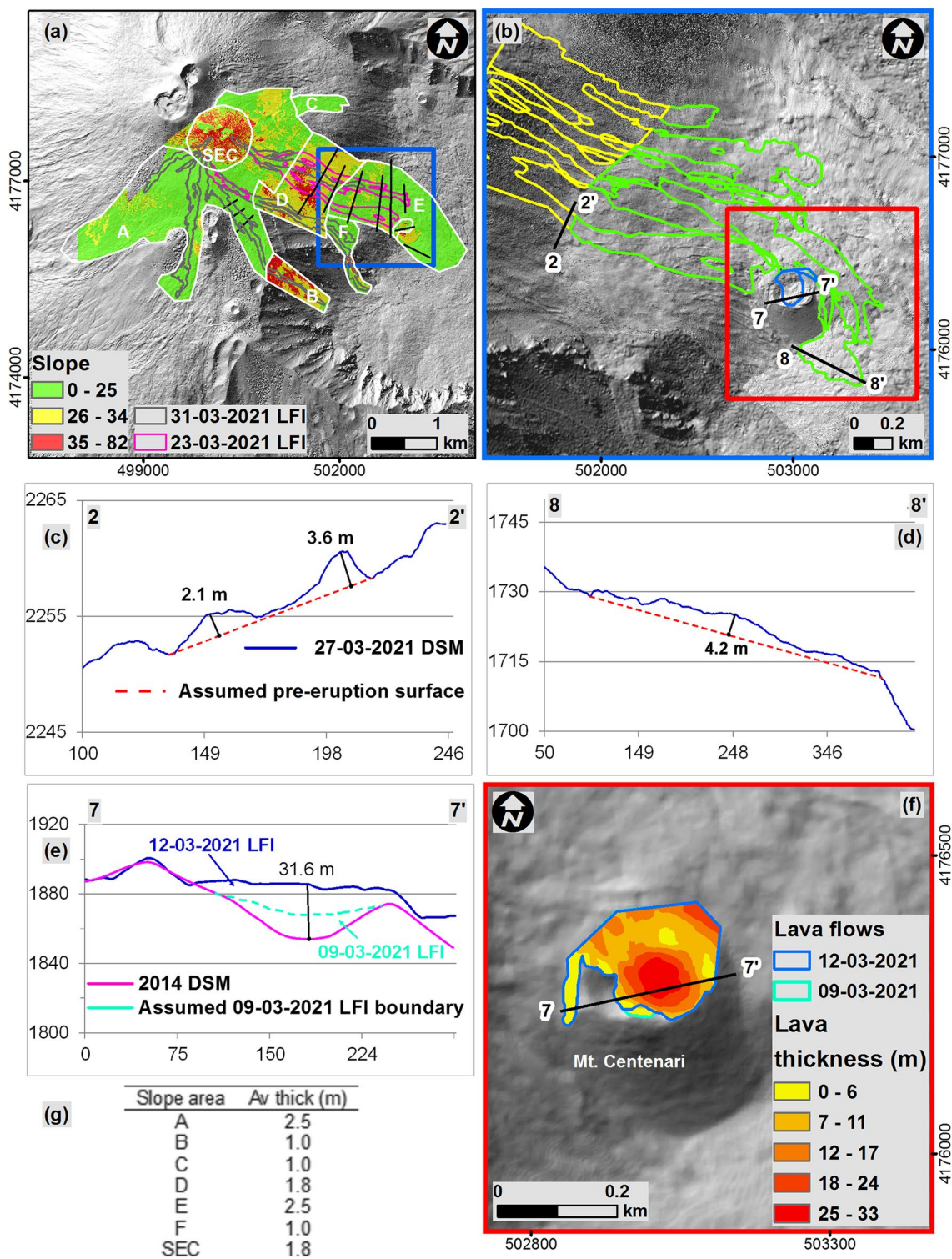


Fig. 3 **a** Slope map superimposed on shaded relief. Fuchsia and grey polygons delimit the lava flows of 23 and 31 March 2021, respectively; white polygons delimit the areas of homogeneous slope, black lines identify the cross-sections measured on the DSM of 27 March 2021, the blue square indicated the area enlarged in panel **b**; **b** limits of the flows for which we estimated the average thicknesses by cross-section, the colours of the polygons correspond to slope areas (see the legend in panel **a**); the red square indicated the area enlarged in

panel **f**; **c**, **d**, **e** examples of cross-sections measured on the 27 March 2021 and 2014 DSMs (blue and fuchsia lines, respectively), the red and turquoise dashed lines indicate the assumed pre-eruption surfaces and the assumed boundary of the 09 March 2021 lava flow (LFI), the black lines and corresponding numbers indicate the maximum thicknesses; **f** thickness of the 09 and 12 March 2021 lava flows inside Mt. Centenari; **g** the table indicates the average flow thickness estimated for each slope area

Table 6 Parameters used

Parameter	Percentage value	Reference
Error on the planimetric evaluation of the volume	20%	Calvari et al. (1994)
Error on the volume evaluated from surface interpolation	40%	De Beni et al. (2019)
Error on the topographic evaluation of the SEC cone volume	4%	Proietti et al. (2020)
Error on the volume evaluated from surface interpolation	40%	De Beni et al. (2019)
Error on the SEC volume evaluated from surface interpolation	4.4%	This work, considering that the 40% error from surface interpolation is applied only to for the 11% of the total volume changes
Error on the total volume changes of SEC cone	8%	This work, sum of the error from interpolation and from topographic evaluation
Error on the total volume changes of SEC cone	20%	This work, conservative estimate considering the different methodologies we combined
Vesicularity of the lava flows	20%	Behncke et al. (2006)
Vesicularity of the SEC cone	50%	Behncke et al. (2006)
Percentage of lava flows, distal and proximal (23%) pyroclasts measured for the 25–26 October 2013 Etna lava fountain	73%, 4% and 23%, respectively	Andronico et al. (2018)

topographic surface. The 2021 DSM does not include the NW portion of the SEC, which corresponds to 35% of the cone basal area (as measured with ESRI ArcGIS). However, this side of the SEC underwent minor morphology changes with respect to the south and east ones because most tephra are generally dispersed towards the SE-ESE by the prevailing westerly wind. The missing elevation changes were estimated by applying the Natural Neighbor interpolation tool of ArcGIS (<https://desktop.arcgis.com/en/arcmap/10.6/management-terrain/hidden-natural-neighbor-interpolation.htm>) to the values measured in adjacent areas of the SEC, where no lava flows were emplaced. The interpolated volume corresponds to 11% of the total volume changes. To improve the quantification of the SEC volume changes, we subtracted the value measured for the portion of lava flows emplaced on the cone to that obtained from the DSM comparison.

In the topographic approach, the maximum volume error is linearly dependent on the standard deviation of the elevation change ($\sigma_{\Delta z}$), calculated from regions where no change occurred (De Beni et al. 2019). However, the September 2021 DSM does not include unchanged areas for measuring $\sigma_{\Delta z}$. This DSM is limited to the SEC cone, which was changed significantly by the paroxysmal events, including its southern base where ballistic and fallout products were deposited. Volume changes of the SEC cone, between 2011 and 2016, were previously measured through the topographic approach, with an associated error of 4% (Proietti et al. 2020). Therefore, we assume that the SEC volume error ranges between 4 and 20%, as previously found for topographic and planimetric

analyses (Table 6). It should also be considered that in the natural neighbor interpolation of a smooth surface, such as that of the NW flank of the SEC, the volume error can be as high as 40% (Table 6; De Beni et al. 2019). Considering that the contribution to SEC volume change measured from data interpolation is 11% of the total change, this gives an error of 4.4%, which should be added to that from topographic analysis, resulting in a total error of about 8%.

The error on volumes evaluated by comparing two point clouds, without GCPs or over an area where no natural change occurred, has been previously estimated with the Cloud Compare software through the Multiscale Model to Model Cloud Comparison and its successive precision map modification (M3C2 and M3C2-PM, Lague et al. 2013; James et al. 2017). We cannot apply the precision map calculation (M3C2-PM) because we do not have precision estimates for the 2020 Pleiades DSM (generated by the MicMac software). We therefore applied the plugin M3C2, considering diameter values between 5 and 20 m for both the normal scale and projection scale and we restricted the differencing to the vertical direction. The obtained distance uncertainties were rasterised to the same spatial resolution of the two DSMs (1 m). However, the obtained confidence intervals are smaller than the 1% of the volume changes evaluated from DSMs comparison.

Ultimately, considering that we calculated the total volume of the SEC cone by combining multiple methodologies with different uncertainties, we believe that an error of 20% (already considered for lava volumes, Table 6) is a conservative estimate for our analysis.

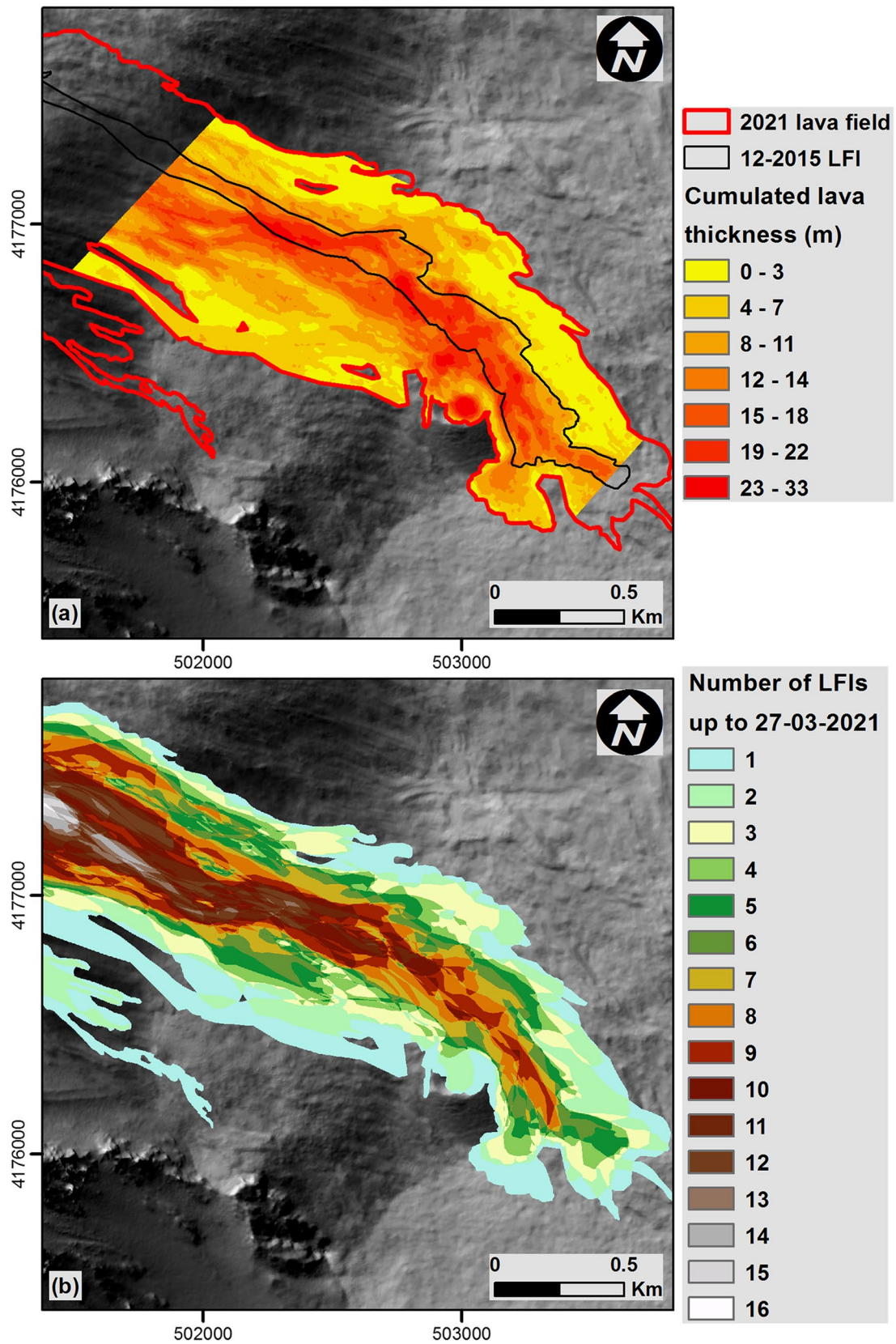


Fig. 4 **a** Cumulative lava thickness of the 2021 lava flows (LFIs) up to the 27 March 2021 plus the December 2015 flow; **b** corresponding resurfacing map that counts the number of accumulated flows

A posteriori analysis of the fallout deposits and ballistics

We measured the thickness of the proximal fallout deposits at the SEC south base by comparing the 16 September 2021 UAS-derived DSM and the 22 August 2020 Pleiades DSM, in ESRI ArcGIS. This deposit accumulated from 53 events (of the 57 paroxysms occurring between the two surveys) with plume dispersion towards the WSW-ESE. The analysis was limited to an area ($\sim 2.7 \times 10^4 \text{ m}^2$) over which the lava flows had not spread.

The thickness of the distal fallout deposits from 27 events (with plume dispersion towards the S-ESE) was determined using DSMs from the two UAS surveys (05 August 2020 and 16 September 2021) above and around the Cisternazza pit crater (Fig. 1 and Table 3), which is about 2.5 km SSE from the SEC. This comparison covered the central flat area inside the Cisternazza ($\sim 0.3 \times 10^4 \text{ m}^2$) and a ring ($\sim 4.0 \times 10^4 \text{ m}^2$) around the pit crater. To estimate the quality of the co-registration between the two datasets, we identified 16 easily recognisable morphological elements, such as overhanging and steep rocks, for which wind would have prevented any fallout deposit accumulating. We measured their 3D coordinates (X, Y and Z) in both DSMs and subtracted the 2020 values from the 2021 values. We obtained mean differences around zero (0.04 m, -0.06 m and -0.02 m for X, Y and Z, respectively), with associated standard deviations of 0.09 m, 0.10 m and 0.14 m. We thus considered 0.14 m as the error associated with thickness measurements in the Cisternazza area.

Finally, we performed a visual analysis of the orthomosaics extracted from the 16 September 2021 UAS survey for an area at the south base of the SEC, between ~ 3050 and 2900 m of elevation. This analysis enabled us to identify ballistics larger than 20 cm and to record their location in a point-type shapefile. Their spatial distribution was then assessed using the Kernel Density tool (in ESRI ArcGIS), which calculates the local neighbourhood feature density.

Quantification of the volume of magma erupted

We measured the bulk volumes of all the lava fields and the changes of the SEC cone due to the 2021 paroxysmal events by applying the cross-section and topographic analyses. We converted bulk volumes to DRE volumes using vesicularity values from the literature of 20% and 50% for the lava flows and the cone, respectively (Behncke et al. 2006, Table 6). A range of vesicularity values has been previously assumed for Etna effusive and explosive products (Andronico et al. 2018) but 20% and 50% values have been used previously for the 2011–2016 SEC eruptive activity, which was similar to 2021 (Behncke et al. 2014; De Beni et al. 2015; Corsaro et al. 2017; Proietti et al. 2020). We also estimated the total DRE volume of distal

tephra by considering the percentage of lava flows (73%), proximal (23%) and distal (4%) pyroclasts previously found for the 25–26 October 2013 event (Andronico et al. 2018, Table 6). The authors proposed that a similar distribution of deposits, showing a predominant output of lava flows and coarse tephra deposited around the cone, with respect to the distal tephra, was observed during the paroxysmal phase of most of the Etna lava fountains (Andronico et al. 2018). We finally combined the DRE volumes measured for the 2021 composite lava flow fields and for the SEC changes with the estimate of the distal fallout deposits, to quantify the DRE volume of the erupted magma.

Results

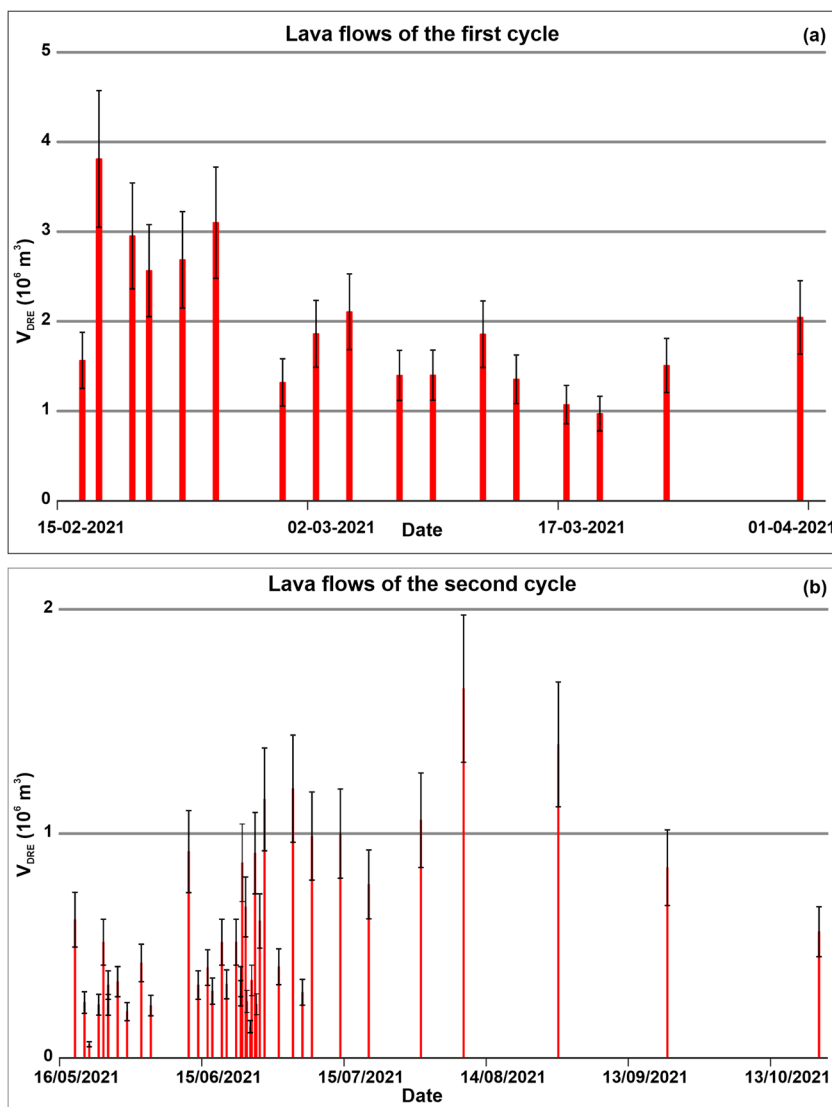
For the first cycle (from 16 February to 1 April) and in the Valle del Bove, we find that the longest lava flow reaching the lowest front elevation (4.3 km and 1700 m a.s.l., respectively) was fed by an effusive vent on 24 February (PE 6, Fig. 2, Table 1 and Table 4). For the same cycle but on the SW flank, the longest lava flow reached the lowest front elevation (3.5 km and 2600 m a.s.l., respectively) on 31 March (PE 17, Table 1 and Table 4). For the second cycle (from 19 May to 23 October), the longest lava flow in the Valle del Bove (2.8 km and 1950 m a.s.l.) was fed by an effusive vent on 09 August (PE 54, Table 2 and Table 5) and for the SW flank (2.9 km and 2350 m a.s.l.) was on 08 July (PE 50, Table 2 and Table 5).

The ranges of the bulk volume of each paroxysm are $(1.2\text{--}4.8) \times 10^6 \text{ m}^3$ and $(0.1\text{--}2.1) \times 10^6 \text{ m}^3$, for the first and the second eruptive cycles, respectively. The corresponding ranges of the DRE volumes are $(1.0\text{--}3.8) \times 10^6 \text{ m}^3$ and $(0.1\text{--}1.6) \times 10^6 \text{ m}^3$, respectively (Table 6, Table 7, and Fig. 5). For the first and the second eruptive cycles, the paroxysmal events that erupted the minimum lava volumes occurred on 19 March and 22 May, respectively. Those that erupted the maximum lava volumes occurred on 17 February and 9 August, respectively (Fig. 5). The bulk volume of the composite lava flow field from the first cycle (17 paroxysms) is $(42 \pm 8) \times 10^6 \text{ m}^3$ and corresponds to an average volume

Table 7 Statistics (minimum, maximum and arithmetic mean) of the average thickness (A_v thick), area (A), bulk and DRE volumes (V_{bulk} and V_{DRE}). These values (including the arithmetic mean of the average thickness) are calculated by considering all the lava flows, and the composite lava field, of the first cycle

I cycle (17 PEs)	A_v thick (m)	A (10^6 m^2)	V_{bulk} (10^6 m^3)	V_{DRE} (10^6 m^3)
Minimum	2.1	0.6	1.2 ± 0.2	1.0 ± 0.2
Maximum	2.5	2.1	4.8 ± 1.0	3.8 ± 0.8
Arithmetic mean	2.2	1.1	2.5 ± 0.5	2.0 ± 0.4
Composite lava field	8.9	4.7	42.0 ± 8.4	33.6 ± 6.7

Fig. 5 DRE volume (V) and corresponding error bar (black lines, calculated as plus or minus 20% of the corresponding value) of each lava flow of the first (a) and second cycle (b); the different ranges of the x and y axes of the two figures were chosen to facilitate the discrimination of individual events



per event of $(2.5 \pm 0.5) \times 10^6 \text{ m}^3$ (Table 7). For the second cycle (40 paroxysms), it is $(29 \pm 6) \times 10^6 \text{ m}^3$ and corresponds to an average volume per event of $(0.7 \pm 0.1) \times 10^6 \text{ m}^3$ (Table 8). These measurements give a total bulk volume for 2021 of $(71 \pm 14) \times 10^6 \text{ m}^3$, corresponding to an average

volume per event of $(1.2 \pm 0.3) \times 10^6 \text{ m}^3$, and a DRE lava volume of $(57 \pm 11) \times 10^6 \text{ m}^3$ (Table 9).

The elevation changes to the SEC scoria cone, derived from comparison of the 16 September 2021 UAS and the 2020 Pleiades DSMs, resulted in a maximum increase of 135 m. The top of the SEC, located on the crest of its south-east rim, reached on 16 September 2021 an altitude of $3348 \pm 1 \text{ m a.s.l.}$ (Fig. 6). The measured changes of the SEC result in

Table 8 Statistics (minimum, maximum and arithmetic mean) of the average thickness (Av thick), area (A), bulk and DRE volumes (V_{bulk} and V_{DRE}). These values (including the arithmetic mean of the average thickness) are calculated by considering all the lava flows, and the composite lava field, of the second cycle

II cycle (40 PEs and 1 EE)	Av thick (m)	A (10^6 m^2)	V_{bulk} (10^6 m^3)	V_{DRE} (10^6 m^3)
Minimum	1.7	0.04	0.1 ± 0.01	0.1 ± 0.01
Maximum	3.1	0.9	2.1 ± 0.4	1.6 ± 0.3
Arithmetic mean	2.2	0.3	0.7 ± 0.1	0.6 ± 0.1
Composite lava field	10.7	2.7	28.8 ± 5.8	23.1 ± 4.6

Table 9 Average thickness (Av thick, evaluated as V_{bulk}/A), area (A), bulk and DRE volumes (V_{bulk} and V_{DRE}) for the composite lava field formed during all the 2021 events and for the SEC cone

2021 (57 PEs and 1 EE)	Av thick (m)	A (10^6 m^2)	V_{bulk} (10^6 m^3)	V_{DRE} (10^6 m^3)
Composite lava field	11.8	5.8	70.8 ± 14.2	56.6 ± 11.3
SEC scoria cone	51	0.7	26.9 ± 5.4	13.5 ± 2.7

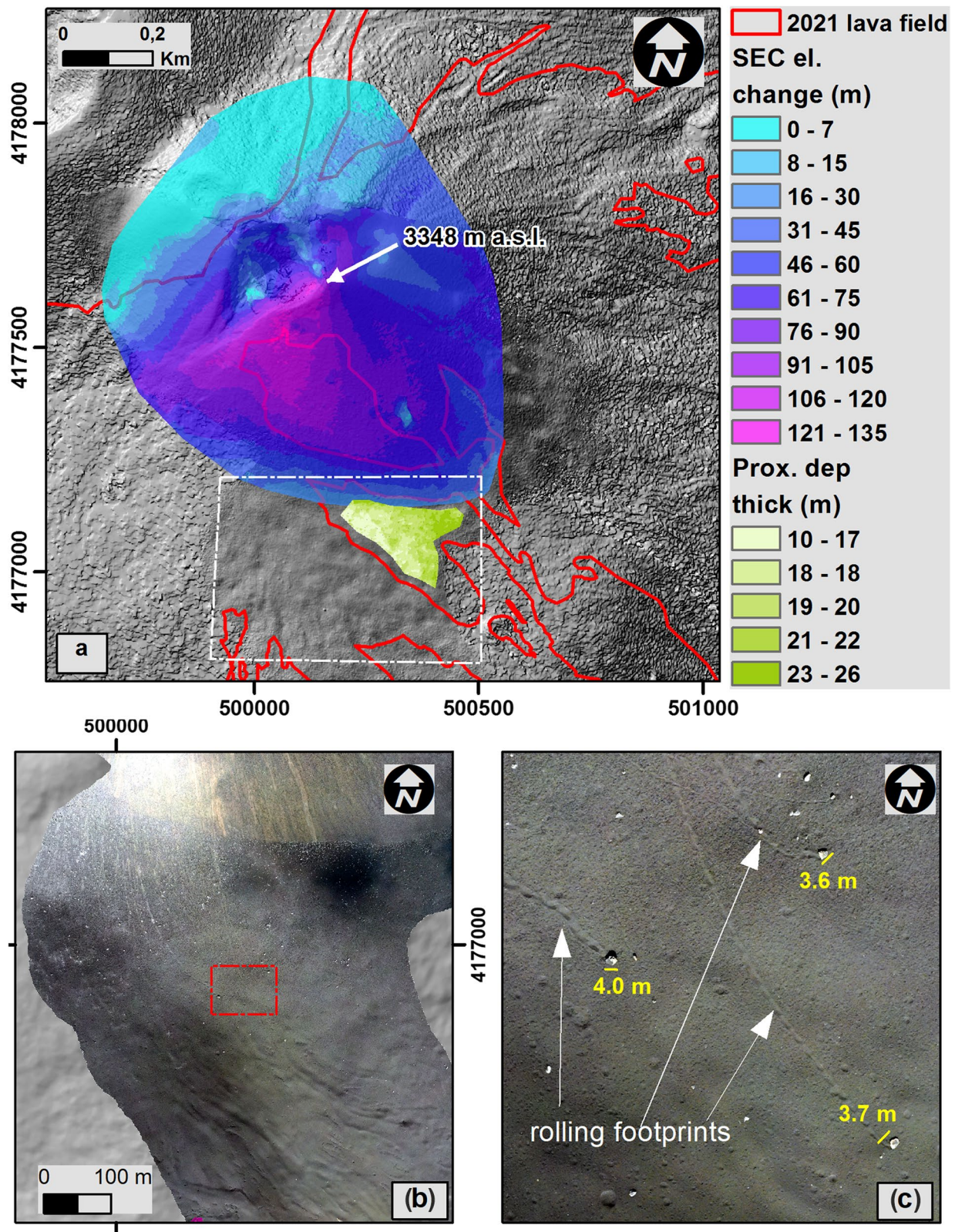


Fig. 6 **a** Elevation change of the SEC cone and thickness of the proximal deposits, the red lines are the limits of the 2021 composite flow field, the white arrow indicate the top of the SEC, and white dashed rectangle delimits the area showed in panel **b**; **b** orthomosaic (16 Sep-

tember 2021) of the lower South flank and base of the SEC showing the ballistics as white spots, the red rectangle delimits the area enlarged in panel **c**; **c** white arrows indicate the rolling footprints of the bigger ballistics

a bulk volume of $(27 \pm 5) \times 10^6 \text{ m}^3$ (Table 9), corresponding to an average volume per event of $(0.5 \pm 0.1) \times 10^6 \text{ m}^3$, and a DRE cone volume of $(13 \pm 3) \times 10^6 \text{ m}^3$ (Table 9). The total DRE volume of magma erupted in 2021 is $(73 \pm 15) \times 10^6 \text{ m}^3$ and it include the lava fields, the SEC change and the estimated distal fallout $(3 \pm 1) \times 10^6 \text{ m}^3$. The combination of the lava flow maps produced for each paroxysm provides the 2021 Etna resurfacing map. This map counts how many times each pixel has been covered during all the 2021 paroxysmal events and provides a quantitative description of the spatio-temporal evolution of the most frequently covered areas (Fig. 8a; an animation of its temporal evolution is available as online resource 1).

The proximal fallout deposits accumulated at the SEC south base have average and maximum thicknesses of 19 and 26 m (Fig. 6a) and become thinner further from the cone. This material was deposited during 53 paroxysms with plume dispersion towards the WSW-ESE, so the corresponding average deposited thickness per event is 0.4 m. The distal fallout from the 27 events with plume dispersion towards the S-ESE was derived from comparison of the 2021 and 2020 DSMs around the Cisternazza pit crater (Fig. 7). Its thickness has a maximum measured value of 3 m in the base of the Cisternazza (average value and standard deviation of 0.80 m and 0.18 m, respectively). This corresponds to an average deposit thickness per event of up to 0.11 m. The fallout is thinnest in the area around the

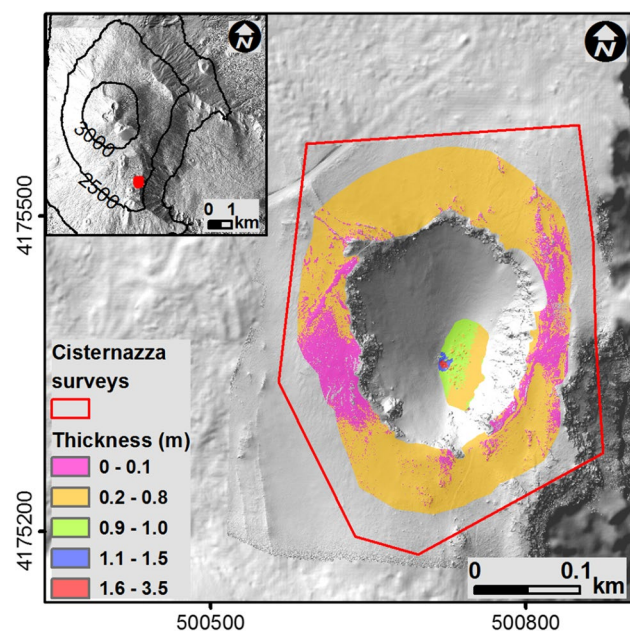


Fig. 7 Thicknesses of the distal deposits measured inside and around the Cisternazza pit crater; the upper left inset locates the Cisternazza surveys (filled red polygon) with respect to the Etna summit area. Background images overlap the 16 September 2021 shaded relief and that of 22 August 2020

pit crater, where the maximum measured value is 0.50 m (average value and standard deviation of 0.15 m and 0.07 m, respectively). This corresponds to an average deposit thickness per event up to 2 cm.

From the analyses of the high-resolution orthomosaic (16 September 2021 UAS survey), we observe that the SEC south base was highly impacted by ballistics. In particular, ballistics between 600 and 900 m from the vent have a discontinuous distribution and a maximum size of 4 m. The larger ones rolled down the slope for at least 750 m (Fig. 6b, c). Moreover, ballistics smaller than 1.5 m are dispersed discontinuously from 900 up to 1200 m from the vent and intercept the tourist track. We present the density map of ballistics drawn for the area at the SEC south base, through a kernel density analysis of the position of ballistics with a linear dimension greater than 0.2 m (Fig. 8b).

Discussion

This work presents the results of the timely mapping of the SEC cone and of the lava flows emplaced on Etna volcano, from 57 paroxysmal events in 2021. These events occurred with a minimum interval of 4 h and mapping was based on the synergistic integration of multi-sensor and multi-platform data, i.e. visible, thermal, near-infrared and SWIR images, acquired from satellites, UAS surveys and the INGV-OE ground-based surveillance cameras. This ensured a constant data flow at multiple spatial and temporal resolutions (from 1.9 cm/px, for UAS orthophotos, to 30 m/px for Landsat-8 orthoimages; from less than 1 day to less than 6 days after an event has occurred), allowing detailed spatial and temporal coverage and understanding of Etna's 2021 eruptive events. The lava flow maps and relative measurements were promptly released to the Italian Civil Protection Department through the "Bollettini and Comunicati" (standardised documents issued by the INGV-OE, to communicate the alert level and briefly describe volcanic activity). We quantify the bulk volume of each lava flow, of the composite flow fields (for the two eruptive cycles and the whole 2021 activity) and of the SEC cone. From these, we derive the average volume per events (for both the flows and the SEC), and the DRE volume of erupted magma. We also measure the average thickness per event of fallout deposits (both proximal and distal). Finally, we evaluate the lava flow resurfacing map and the density map of ballistics at the SEC south base.

The higher average volume per event measured for the first cycle with respect to the second one ($2.5 \times 10^6 \text{ m}^3$ versus $0.7 \times 10^6 \text{ m}^3$) is mainly due to the February paroxysms that erupted almost double the lava volume of the subsequent events. In March 2021, erupted volumes decreased but they were still generally greater than those of the second

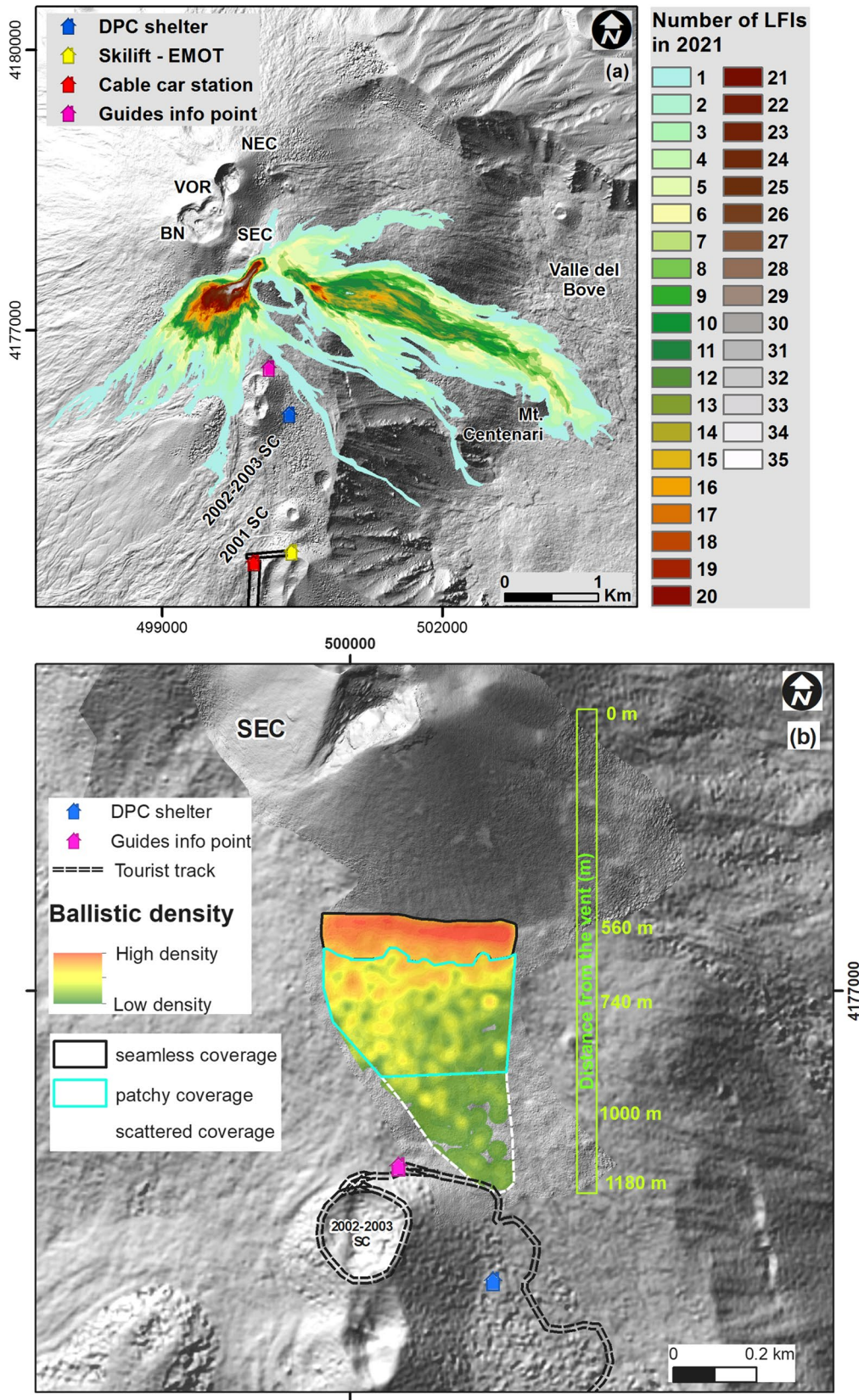


Fig. 8 **a** Resurfacing map and location of anthropogenic features; **b** kernel density map of ballistics deposited at the SEC south base. Background images overlap the 16 September 2021 shaded relief and that of 22 August 2020

cycle (Fig. 5). The total DRE volume of magma erupted during the 57 SEC paroxysms (16 February–23 October 2021) is $(73 \pm 15) \times 10^6 \text{ m}^3$ and corresponds to an average output rate of about $3.4 \text{ m}^3/\text{s}$. This value is higher than the corresponding values measured between 22 August 2020 and 29 June 2022 (2.88; Ganci et al. 2023) and much higher than Etna's long-term steady state output ($0.8\text{--}0.9 \text{ m}^3/\text{s}$; Wadge and Guest 1981; Bonaccorso and Calvari 2013). However, the 2021 higher output rate can be explained by the low eruptive activity observed between 26 May 2016 (end of the 2011–2016 eruptive period, Proietti et al. 2020) and 17 February 2021 (before the beginning of the 2021 first eruptive cycle). In this period, Etna produced only short-lived lava flows and five paroxysms. The erupted total DRE volume is less than $30 \times 10^6 \text{ m}^3$ (Cappello et al. 2019; De Beni et al. 2021; “Bollettino Etna” (n.d.) which is much lower than the value estimable for a steady-state accumulation over a period of about 4.7 years (Bonaccorso and Calvari 2013).

The high-resolution DSM extracted from the 16 September 2021 UAS survey (Table 3) enabled us to measure that the SEC cone summit (3348 m a.s.l.) is the new peak of Etna volcano (Fig. 6), now higher than the NEC ($3321 \pm 1 \text{ m a.s.l.}$, in the 2020 DSM).

Our resurfacing map shows that, at the end of the 2021 eruptive activity, the most affected area was the southwest base of the SEC, where up to 35 flows overlap. This zone is less than 1 km from the guides' information point, which is frequently visited by tourists, that is to Fig. 8a. This result highlights the need to provide near real-time monitoring and forecasting data to civil protection authorities. Such information is pivotal for managing access for volcanologists, stakeholders, and tourists and mitigating the hazard related to summit lava flows. In fact, summit lava flows are slow enough to allow people to move away from their fronts but, in some cases, they can be hazardous to any people near them. For example, the interaction between lava flows and snow or water can create localised phreatic explosions (Chester et al. 1985; Blong 1984). The resurfacing map could support the assessment of the areas most exposed to inundation by Etna's summit lava flows and can be used as input and checking data of lava flow numerical models (Del Negro et al. 2013).

The density map of ballistics (Fig. 8b) should only be interpreted qualitatively because it underestimates the actual ballistics number density. Many ballistics have been mantled subsequently by ash and lapilli deposition. In addition, on impact, many ballistics break into parts too small to be identified in the orthophoto. Nevertheless, the density map highlights the risk associated with ballistics especially near the tourist track that was intercepted at about 2900 m. Our analysis shows that the SEC south base, which is close to the tourist footpaths leading to the 2002–2003 scoria cones and the summit craters, was highly impacted. These results

could support studies aimed at modelling the trajectories of ballistics during lava fountains, with the aim of identifying the affected area in near real-time and quantifying the hazard (Alatorre-Ibargüengoitia et al. 2012; Fitzgerald et al. 2017 and 2014; Spanu et al. 2016; Costa et al. 2023).

The measured maximum thickness of the distal fallout deposits around the Cisternazza pit crater (0.50 m) has the same order of magnitude as its (0.14 m) error. This small accumulation could be due to tephra remobilisation by strong winds. Greater thicknesses, ranging between 0.50 and 3.00 m, have accumulated on the lowest portion of the Cisternazza pit crater. However, these are likely influenced by the funnel-like crater geometry, with steep walls up to 60 m deep, acting as a natural collector for both fallout and reworked deposits, as well as the debris material eventually detached from the boundary walls.

Our volume estimates align with those of previous work on 2021 Etna's eruptive activity. The bulk volume ($71 \times 10^6 \text{ m}^3$) we obtained for the composite lava field formed during the 2021 paroxysms is in agreement with its recent estimates from Pleiades DSMs (Ganci et al. 2022, 2023). This value is also comparable to that measured for long-lived (420 days) lateral eruptions, i.e. during 2008–2009 (Ganci et al. 2012). We also note that the volume estimates for each of the 2021 lava flows are well within the range of uncertainties of the corresponding values estimated from thermal satellite data (Ganci et al. 2023). The bulk lava volume we measured for the 12 March event ($2.3 \pm 0.5 \times 10^6 \text{ m}^3$) is compatible with that ($2.4 \times 10^6 \text{ m}^3$) measured previously by analysing the strain changes, the images acquired from the INGV-OE surveillance cameras, and satellite data (Calvari et al. 2021). The total volume erupted by the Etna lava fountains of February–March 2021 was previously estimated as $52.5 \times 10^6 \text{ m}^3$ from strain changes measured by high-precision borehole dilatometers (Bonaccorso et al. 2021). This result is compatible with our DRE magma volume estimate for the first cycle ($43 \pm 9 \times 10^6 \text{ m}^3$), by adding the value measured for lava flows and that extrapolated for the SEC. The latter is obtained by redistributing the overall 2021 volume of the SEC based on the ratio between the lava volumes measured for the first cycle and all the 2021 events through:

$$V_{SEC}^{I \text{ cycle}} = V_{SEC}^{tot} \frac{V_{lava}^{I \text{ cycle}}}{V_{lava}^{tot}}$$

where the subscript *SEC* or *lava* indicates that the volume (*V*) refers to the SEC or lava flows, respectively, whereas the superscript *I cycle* or *tot* indicates that the volume (*V*) is related to the events of the first cycle or all the 2021 events, respectively.

The 2021 activity (average volumes per event of $1.2 \times 10^6 \text{ m}^3$ and $0.5 \times 10^6 \text{ m}^3$ for the lava flows and the SEC, respectively) can be compared with the 50 paroxysms occurring

in 2011–2014. The 2011–2014 bulk volumes for lava flows and the New South-East Crater (NSEC) were $84 \times 10^6 \text{ m}^3$ and $50 \times 10^6 \text{ m}^3$, respectively, with corresponding average volumes per event of $1.7 \times 10^6 \text{ m}^3$ and $1.0 \times 10^6 \text{ m}^3$ (De Beni et al. 2015). Although the lava flow volume per event estimates are similar, estimates of average SEC volume increase per event in 2021 are approximately half of those for 2011–2014. This difference could be explained by both the changing conditions of cone growth and the timing between 2011 and 2014 compared with 2021. In 2011, the NSEC started to grow from a small pit crater (about $5 \times 9 \text{ m}$) on the lower east flank of the “old” SEC. The proximal pyroclastic deposits accumulated into a scoria cone of comparable size to the old one (Behncke et al. 2014; De Beni et al. 2015). During 2011–2014, the time intervals between consecutive events were longer than those in 2021, allowing the NSEC to be more stable than the SEC. The only lateral collapse occurred on 11 February 2014 (Andronico et al. 2018), when the NSEC cone had equalled in size the old SEC. From 13 December 2020, there were several lateral collapses of the SEC, due to the formation of fractures, combined with a frequent explosive activity, which weakened its east and south summit areas. The lateral collapses were associated with pyroclastic flows (on 16 February, 28 February, 24 March and 23 October). The 2021 proximal pyroclastic deposits accumulated on a yet-constructed cone whose flanks, having an average slope of 30% (measured from the UAS DSMs), had already reached the repose angle for dry pyroclastic deposits (32–33%, Wood 1980). Therefore, the cone could no longer accumulate further considerable volumes of pyroclastic products, which flowed down and accumulated at its base, where the slope decreases. This hypothesis is supported by the proximal deposit thickness measured at the lower SE flank of the SEC, ranging between 10 and 26 m (Fig. 6a). It is also reasonable to hypothesise that a large part of the deposits flowed into the Valle del Bove.

Our analyses confirm that the integration of satellite data with those acquired from other platforms (UAS and ground cameras) makes it possible to monitor eruptive events whose frequency is greater than the satellite’s revisit time. The analysis of thermal images, acquired from one of the three remote platforms, in addition to visible images, makes it possible to distinguish active lava flows from recent cooling ones, especially when the eruption frequency is high (e.g. up to three events in the same day). UAS can provide valuable data for volcano monitoring. However, it must always be assessed whether the level of volcanic activity and weather conditions permit a flight. Weather conditions can change very quickly, going from sunny to overcast or foggy in a matter of minutes. Such abrupt changes could compromise flight performance and survey results and, in

the worst case, cause a loss of control of the drone. Thus, automated return-to-base is a valuable capability for a UAS. Low temperatures (e.g. $-10 \text{ }^\circ\text{C}$, or lower) and moderate to very-high-speed wind (more than 20 knots, 37 km/h) can reduce battery capacity by up to 50% and require surveys to be split into multiple flights. A strong knowledge of the volcano and expertise in piloting in extreme conditions are required to maximise survey success. Finally, even if fixed ground-based cameras allow observation of only some areas of the volcano’s flanks, their real-time image acquisition supports volcano surveillance and mapping when satellite and UAS data are not available.

Conclusions

The integration of multi-sensor and multi-platform remote sensing data has proven effective in monitoring and quantifying high-frequency eruptive events, such as the 2021 Etna paroxysms (with up to three events in one day). Rapid results from our analysis, which were promptly released to the Italian Civil Protection Department, are the lava flow maps for most of the eruptive events and the measurement of the related geometric parameters. We also released three datasets that could support further quantification of the hazard from summit eruptions, namely the 2021 Etna’s resurfacing map, its temporal evolution and the ballistics density map. Further outcomes are the quantification of the bulk volumes for the lava field, and the change of the SEC cone, and the corresponding DRE values. The comparability of the 2021 volume with that of the 2008–2009 eruption, the high output rate of the 2021 paroxysms and the low volume erupted in the previous period (26 May 2016–17 February 2021) lead us to conclude that the occurrence of a repeated series of many low-volume events is sufficient to restore the volcano’s equilibrium state, analogously to a long-lasting lateral eruption. Therefore, by the end of 2021, Etna volcano has reached its equilibrium state. Thereafter, there have been only two paroxysmal events, in February 2022, two mild and purely effusive eruptions in Valle del Bove and Valle del Leone (11 May–13 June 2022 and 27 November 2022–7 February 2023) and two paroxysmal events in May and August 2023. To date, 2 months after the last event, the volcano only shows mild degassing. The methodology implemented during the 2021 paroxysm monitoring is also applicable to a potential lateral eruption of Etna. In this case, mapping and quantification of erupted products would be more urgent, as such flows could arrive near inhabited areas, posing a greater risk than summit eruptions. Our strategy can be exported to other volcanoes and extended to different environmental monitoring.

Supplementary Information The online version contains supplementary material available at <https://doi.org/10.1007/s00445-023-01673-w>.

Acknowledgements We would like to thank the scientists and technicians from INGV-OE for the maintenance of camera and GPS monitoring networks. G.G. thanks to the research project “TUNE – Effusion rate estimates at Etna and Stromboli: constraints imposed by a variety of satellite remote sensing data” (Bando di Ricerca Libera 2019 of INGV). We would like to thank the associated editor Mike James for handing the paper, the Executive Editor, the two anonymous referees and the referee Michael Ramsey for their suggestions that helped improving the clarity of the paper.

Funding Open access funding provided by Istituto Nazionale di Geofisica e Vulcanologia within the CRUI-CARE Agreement. This work was supported by funding provided by the Italian Presidenza del Consiglio dei Ministri—Dipartimento della Protezione Civile (DPC), All. A and All. B2-Task 11 “Real-time quantification of Etna’s eruptive activity from fixed thermal cameras and satellite data” (Scientific Responsibility: G.G.). This paper does not necessarily represent DPC official opinion and policies.

Data availability The camera and GPS data used in this study are property of INGV-OE (Istituto Nazionale di Geofisica e Vulcanologia - Osservatorio Etneo, Sezione di Catania). The Sentinel-2 MSI, Landsat-8 OLI and TIRS satellite data analysed in this study are openly available through the Sentinel Hub services (<https://www.sentinel-hub.com/> accessed on 11 September 2022) for Copernicus Sentinel data. Skysat images were provided by Planet Labs PBC under Academic licence.

Declarations

Conflict of interest The authors declare no competing interests.

Open Access This article is licensed under a Creative Commons Attribution 4.0 International License, which permits use, sharing, adaptation, distribution and reproduction in any medium or format, as long as you give appropriate credit to the original author(s) and the source, provide a link to the Creative Commons licence, and indicate if changes were made. The images or other third party material in this article are included in the article's Creative Commons licence, unless indicated otherwise in a credit line to the material. If material is not included in the article's Creative Commons licence and your intended use is not permitted by statutory regulation or exceeds the permitted use, you will need to obtain permission directly from the copyright holder. To view a copy of this licence, visit <http://creativecommons.org/licenses/by/4.0/>.

References

- Acocella V, Neri M, Behncke B, Bonforte A, Del Negro C, Ganci G (2016) Why does a mature volcano need new vents? The case of the New Southeast Crater at Etna. *Front Earth Sci* 4:67. <https://doi.org/10.3389/feart.2016.00067>
- Alatorre-Ibargüengoitia MA, Delgado-Granados H, Dingwell DB (2012) Hazard map for volcanic ballistic impacts at Popocatepetl volcano (Mexico). *Bull Volcanol* 74:2155–2169. <https://doi.org/10.1007/s00445-012-0657-2>
- Allard P, Behncke B, D’Amico S, Neri M, Gambino S (2006) Mount Etna 1993–2005: anatomy of an evolving eruptive cycle. *Earth Sci Rev* 78(1–2):85–114. <https://doi.org/10.1016/j.earscirev.2006.04.002>

- Alparone S, Andronico D, Lodato L, Sgroi T (2003) Relationship between tremor and volcanic activity during the Southeast Crater eruption on Mount Etna in early 2000. *Journal of Geophysical Research: Solid Earth* 108(B5). <https://doi.org/10.1029/2002JB001866>
- Alsadik B, Remondino F (2020) Flight planning for LiDAR-based UAS mapping applications. *ISPRS Int J Geo Inf* 9(6):378. <https://doi.org/10.3390/ijgi9060378>
- Aloisi M, D’Agostino M, Dean KG, Mostaccio A, Neri G (2002) Satellite analysis and PUFF simulation of the eruptive cloud generated by the Mount Etna paroxysm of 22 July 1998. *J Geophys Res Solid Earth* 107(B12):ECV–EC9. <https://doi.org/10.1029/2001JB000630>
- Andaru R, Rau JY, Syahbana DK, Prayoga AS, Purnamasari HD (2021) The use of UAV remote sensing for observing lava dome emplacement and areas of potential lahar hazards: an example from the 2017–2019 eruption crisis at Mount Agung in Bali. *J Volcanol Geotherm Res* 415:107255. <https://doi.org/10.1016/j.jvolgeores.2021.107255>
- Andronico D, Scollo S, Cristaldi A, Lo Castro MD (2014) Representativity of incompletely sampled fall deposits in estimating eruption source parameters: a test using the 12–13 January 2011 lava fountain deposit from Mt Etna volcano, Italy. *Bull Volcanol* 76(10):1–14. <https://doi.org/10.1007/s00445-014-0861-3>
- Andronico D, Scollo S, Cristaldi A (2015) Unexpected hazards from tephra fallouts at Mt Etna: the 23 November 2013 lava fountain. *J Volcanol Geotherm Res* 304:118–125. <https://doi.org/10.1016/j.jvolgeores.2015.08.007>
- Andronico D, Behncke B, De Beni E, Cristaldi A, Scollo S, Lopez M, Lo Castro MD (2018) Magma budget from lava and tephra volumes erupted during the 25–26 October 2013 lava fountain at Mt Etna. *Front Earth Sci* 6:116. <https://doi.org/10.3389/feart.2018.00116>
- Andronico D, Cannata A, Di Grazia G, Ferrari F (2021) The 1986–2021 paroxysmal episodes at the summit craters of Mt. Etna: insights into volcano dynamics and hazard. *Earth Sci Rev* 220:103686. <https://doi.org/10.1016/j.earscirev.2021.103686>
- Bagnardi M, González PJ, Hooper A (2016) High-resolution digital elevation model from tri-stereo Pleiades satellite imagery for lava flow volume estimates at Fogo Volcano. *Geophys Res Lett* 43:6267–6275. <https://doi.org/10.1002/2016GL069457>
- Baldi P, Bonvalot S, Briole P, Marsella M (2000) Digital photogrammetry and kinematic GPS applied to the monitoring of Vulcano Island, Aeolian Arc Italy. *Geophys J Int* 142(3):801–811. <https://doi.org/10.1046/j.1365-246x.2000.00194.x>
- Barsotti S, Andronico D, Neri A, Del Carlo P, Baxter PJ, Aspinall WP, Hincks T (2010) Quantitative assessment of volcanic ash hazards for health and infrastructure at Mt. Etna (Italy) by numerical simulation. *J Volcanol Geotherm Res* 192(1–2):85–96. <https://doi.org/10.1016/j.jvolgeores.2010.02.011>
- Barsotti S, Parks MM, Pfeffer MA, Óladóttir BA, Pedersen GBM, Jónsdóttir K, Oddsson B (2022) Communicating volcanic hazard during the 2021 Fagradalsfjall eruption in Iceland: from science to operations. 5a Conferenza A Rittmann Catania. <https://doi.org/10.13127/misc/70>
- Behncke B, Neri M, Carniel R (2003) An exceptional case of endogenous lava dome growth spawning pyroclastic avalanches: the 1999 Bocca Nuova eruption of Mt. Etna (Italy). *J Volcanol Geotherm Res* 124(1–2):115–128. [https://doi.org/10.1016/S0377-0273\(03\)00072-6](https://doi.org/10.1016/S0377-0273(03)00072-6)
- Behncke B, Neri M (2003) Cycles and trends in the recent eruptive behaviour of Mount Etna (Italy). *Can J Earth Sci* 40(10):1405–1411. <https://doi.org/10.1139/e03-052>
- Behncke B, Neri M, Pecora E, Zanon V (2006) The exceptional activity and growth of the Southeast Crater, Mount Etna

- (Italy), between 1996 and 2001. *Bull Volcanol* 69(2):149–173. <https://doi.org/10.1007/s00445-006-0061-x>
- Behncke B (2009) Hazards from pyroclastic density currents at Mt. Etna (Italy). *J Volcanol Geotherm Res* 180(2–4):148–160. <https://doi.org/10.1016/j.jvolgeores.2008.09.021>
- Behncke B, Branca S, Corsaro RA, De Beni E, Miraglia L, Proietti C (2014) The 2011–2012 summit activity of Mount Etna: birth, growth and products of the new SE crater. *J Volcanol Geotherm Res* 270:10–21. <https://doi.org/10.1016/j.jvolgeores.2013.11.012>
- Blong RJ (1984) *Volcanic hazards: a sourcebook on the effects of eruptions*. Academic Press, Sydney, p 484
- Bollettino Etna (n.d.) <https://www.ct.ingv.it/index.php/monitoraggio-e-sorveglianza/prodotti-del-monitoraggio/bollettini-setti-manali-multidisciplinari?filter%5Bsearch%5D=Etna> Accessed 12 September 2022
- Bombrun M, Spampinato L, Harris A, Barra V, Caltabiano T (2016) On the transition from Strombolian to fountaining activity: a thermal energy-based driver. *Bull Volcanol* 78:15. <https://doi.org/10.1007/s00445-016-1009-4>
- Bonaccorso A, Calvari S (2013) Major effusive eruptions and recent lava fountains: balance between expected and erupted magma volumes at Etna volcano. *Geophys Res Lett* 40:6069–6073. <https://doi.org/10.1002/2013GL058291>
- Bonaccorso A, Carleo L, Currenti G, Sicali A (2021) Magma migration at shallower levels and lava fountains sequence as revealed by borehole dilatometers on Etna Volcano. *Front Earth Sci* 9:740505. <https://doi.org/10.3389/feart.2021.740505>
- Branca S, Del Carlo P (2005) Types of eruptions of Etna volcano AD 1670–2003: implications for short-term eruptive behaviour. *Bull Volcanol* 67(8):732–742. <https://doi.org/10.1007/s00445-005-0412-z>
- Branca S, De Beni E, Proietti C (2013) The large and destructive 1669 AD eruption at Etna volcano: reconstruction of the lava flow field evolution and effusion rate trend. *Bull Volcanol* 75:1–16
- Caballero I, Román A, Tovar-Sánchez A, Navarro G (2022) Water quality monitoring with Sentinel-2 and Landsat-8 satellites during the 2021 volcanic eruption in La Palma (Canary Islands). *Sci Total Environ* 822. <https://doi.org/10.1016/j.scitotenv.2022.153433>
- Calvari S, Coltelli M, Neri M, Pompilio M, Scrivano V (1994) The 1991–1993 Etna eruption: chronology and lava flow-field evolution. *Acta Vulcanol* 4:1–14
- Calvari S, Bonaccorso A, Ganci G (2021) Anatomy of a paroxysmal lava fountain at Etna Volcano: the case of the 12 March, 2021 Episode. *Remote Sens* 13:3052. <https://doi.org/10.3390/rs13153052>
- Calvari S, Nunnari G (2022) Comparison between automated and manual detection of lava fountains from fixed monitoring thermal cameras at Etna Volcano Italy. *Remote Sensing* 14(10):2392 <https://www.mdpi.com/2072-4292/14/10/2392>
- Cappello A, Neri M, Acocella V, Gallo G, Vicari A, Del Negro C (2012) Spatial vent opening probability map of Etna volcano (Sicily, Italy). *Bull Volcanol* 74:2083–2094. <https://doi.org/10.1007/s00445-012-0647-4>
- Cappello A, Ganci G, Bilotta G, Héroult A, Zago V, Del Negro C (2019) Satellite-driven modeling approach for monitoring lava flow hazards during the 2017 Etna eruption. *Ann Geophys* 62:2. <https://doi.org/10.4401/ag-7792>
- Carr BB, Clarke AB, Arrowsmith JR, Vanderkluyzen L, Dhanu BE (2019) The emplacement of the active lava flow at Sinabung Volcano, Sumatra, Indonesia, documented by structure-from-motion photogrammetry. *J Volcanol Geotherm Res*. <https://doi.org/10.1016/j.jvolgeores.2018.02.004>
- Carr BB, Lev E, Vanderkluyzen L, Moyer D, Marliyani GI, Clarke AB (2022) The stability and collapse of lava domes: insight from photogrammetry and slope stability models applied to Sinabung Volcano (Indonesia). *Front Earth Sci*. <https://doi.org/10.3389/feart.2022.813813>
- Chester DK, Duncan AM, Guest JE, Kilburn CRJ (1985) *Mount Etna: the anatomy of a volcano*. Chapman and Hall, London, p 404
- Chevrel MO, Favalli M, Villeneuve N, Harris AJ, Fornaciai A, Richter N, Derrien A, Boissier P, Di Muro A, Peltier A (2021) Lava flow hazard map of Piton de la Fournaise volcano. *Nat Hazards Earth Syst Sci* 21(8):2355–2377. <https://doi.org/10.5194/nhess-21-2355-2021>
- Chevrel MO, Harris A, Peltier A, Villeneuve N, Coppola D, Gouhier M, Drenne S (2022) Volcanic crisis management supported by near real-time lava flow hazard assessment at Piton de la Fournaise. *La Réunion Volcanica* 5(2):313–334. <https://doi.org/10.30909/vol.05.02.313334>
- Civico R, Ricci T, Scarlato P, Andronico D, Cantarero M, Carr BB, De Beni E, Del Bello E, Johnson JB, Kueppers U, Pizzimenti L, Schmid M, Strehlow K, Taddeucci J (2021) Unoccupied Aircraft Systems (UASs) Reveal the morphological changes at Stromboli volcano (Italy) before, between, and after the 3 July and 28 August 2019 paroxysmal eruptions. *Remote Sens* 13(15):2870. <https://doi.org/10.3390/rs13152870>
- Civico R, Ricci T, Scarlato P, Taddeucci J, Andronico D, Del Bello E, D’Auria L, Hernández PA PNM (2022) High-resolution digital surface model of the 2021 eruption deposit of Cumbre Vieja volcano, La Palma. *Spain Sci Data* 9:435. <https://doi.org/10.1038/s41597-022-01551-8>
- Coltelli M, D’Aranno PJV, De Bonis R, Guerrero F, Marsella M, Nardinocchi C, Pecora E, Proietti C, Scifoni S, Scutti M, Wahbeh W (2017) The use of surveillance cameras for the rapid mapping of lava flow: an application to Mount Etna Volcano. *Remote Sens* 9:192. <https://doi.org/10.3390/rs9030192>
- Corsaro RA, Andronico D, Behncke B, Branca S, De Beni E, Caltabiano T, Ciancitto F, Cristaldi A, De Beni E, La Spina A, Lodato L, Miraglia L, Neri M, Salerno G, Scollo S, Spata G (2017) Monitoring the December 2015 summit eruptions of Mt. Etna (Italy): implications on eruptive dynamics. *J Volcanol Geotherm Res* 341:53–69. <https://doi.org/10.1016/j.jvolgeores.2017.04.018>
- Corsaro RA, Miraglia L (2022) Near real-time petrologic monitoring on volcanic glass to infer magmatic processes during the February–April 2021 paroxysms of the south-east crater, Etna. *Front Earth Sci*. <https://doi.org/10.3389/feart.2022.828026>
- Costa G, Mereu L, Prestifilippo M, Scollo S, Viccaro M (2023) Modeling the trajectories of ballistics in the summit area of Mt. Etna (Italy) during the 2020–2022 sequence of lava fountains. *Geosciences* 13(5):145. <https://doi.org/10.3390/geosciences13050145>
- De Beni E, Behncke B, Branca S, Nicolosi I, Carluccio R, D’Ajello Caracciolo F, Chiappini M (2015) The continuing story of Etna’s New Southeast Crater (2012–2014): evolution and volume calculations based on field surveys and aerophotogrammetry. *J Volcanol Geotherm Res* 303:175–186. <https://doi.org/10.1016/j.jvolgeores.2015.07.021>
- De Beni E, Cantarero M, Messina A (2019) UAVs for volcano monitoring: a new approach applied on an active lava flow on Mt. Etna (Italy), during the 27 February–02 March 2017 eruption. *J Volcanol Geotherm Res* 369:250–262. <https://doi.org/10.1016/j.jvolgeores.2018.12.001>
- De Beni E, Cantarero M, Neri M, Messina A (2021) Lava flows of Mt Etna, Italy: the 2019 eruption within the context of the last two decades (1999–2019). *J Maps* 17(3):65–76. <https://doi.org/10.1080/17445647.2020.1854131>
- Del Negro C, Cappello A, Neri M, Bilotta G, Héroult A, Ganci G (2013) Lava flow hazards at Mount Etna: constraints imposed by eruptive history and numerical simulations. *Sci Rep* 3:3493. <https://doi.org/10.1038/srep03493>

- Diefenbach AK, Crider JG, Schilling SP et al (2012) Rapid, low-cost photogrammetry to monitor volcanic eruptions: an example from Mount St. Helens, Washington, USA. *Bull Volcanol* 74:579–587. <https://doi.org/10.1007/s00445-011-0548-y>
- Dietterich HR, Lev E, Chen J, Richardson JA, Cashman KV (2017) Benchmarking computational fluid dynamics models of lava flow simulation for hazard assessment, forecasting, and risk management. *J Appl Volcanol* 6:9. <https://doi.org/10.1186/s13617-017-0061-x>
- Dietterich HR, Diefenbach AK, Soule SA, Zoeller MH, Patrick MP, Major JJ, Lundgren PR (2021) Lava effusion rate evolution and erupted volume during the 2018 Kilauea lower East Rift Zone eruption. *Bull Volcanol* 83:1–18. <https://doi.org/10.1007/s00445-021-01443-6>
- Di Traglia F, Fornaciai A, Favalli M, Nolesini T, Casagli N (2020) Catching geomorphological response to volcanic activity on steep slope volcanoes using multi-platform remote sensing. *Remote Sens* 12(3):438. <https://doi.org/10.3390/rs12030438>
- Donnadieu F, Freville P, Hervier C, Coltelli M, Scollo S, Prestifilippo M, Valade S, Rivet S, Caucal P (2016) Near-source Doppler radar monitoring of tephra plumes at Etna. *J Volcanol Geotherm Res* 312:26–39. <https://doi.org/10.1016/j.jvolgeores.2016.01.009>
- Dvigalo V, Shevchenko A, Svirid I (2016) Photogrammetric survey in volcanology: a case study for Kamchatka active volcanoes. In: Nemeth K (ed) *Updates in volcanology - from volcano modelling to volcano geology*. InTech, pp 55–79. <https://doi.org/10.5772/63577>
- Ernst GGJ, Kervyn M, Teeuw RM (2008) Advances in the remote sensing of volcanic activity and hazards, with special consideration to applications in developing countries. *Int J Remote Sens* 29(22):6687–6723. <https://doi.org/10.1080/01431160802168459>
- Falsaperla S, Neri M (2015) Seismic footprints of shallow dyke propagation at Etna Italy. *Sci Rep* 5(1):1–9. <https://doi.org/10.1038/srep11908>
- Favalli M, Karátson D, Mazzarini F, Pareschi MT, Boschi E (2009) Morphometry of scoria cones located on a volcano flank: a case study from Mt. Etna (Italy), based on high-resolution LiDAR data. *J Volcanol Geotherm Res* 186(3–4):320–330. <https://doi.org/10.1016/j.jvolgeores.2009.07.011>
- Favalli M, Fornaciai A, Nannipieri L, Lormand C (2018) UAV-based remote sensing surveys of lava flow fields: a case study from Etna's 1974 channel-fed lava flows. *Bull Volcanol* 80:29. <https://doi.org/10.1007/s00445-018-1192-6>
- Felpeto A, Martí J, Ortiz R (2007) Automatic GIS-based system for volcanic hazard assessment. *J Volcanol Geotherm Res* 166(2):106–116. <https://doi.org/10.1016/j.jvolgeores.2007.07.008>
- Fitzgerald RH, Tsunematsu K, Kennedy BM, Breard ECP, Lube G, Wilson TM, Jolly AD, Pawson J, Rosenberg MD, Cronin SJ (2014) The application of a calibrated 3D ballistic trajectory model to ballistic hazard assessments at Upper Te Maari, Tongariro. *J Volcanol Geotherm Res* 286:248–262. <https://doi.org/10.1016/j.jvolgeores.2014.04.006>
- Fitzgerald RH, Kennedy BM, Wilson TM, Leonard GS, Tsunematsu K, Keys H (2017) The communication and risk management of volcanic ballistic hazards. In: Fearnley CJ, Bird DK, Haynes K, McGuire WJ, Jolly G (eds) *Observing the Volcano World*. *Advances in Volcanology*. Springer, Cham. https://doi.org/10.1007/11157_2016_35
- Francis PW (1979) Infra-red techniques for volcano monitoring and prediction—a review. *J Geol Soc* 136(3):355–359
- Francis PW, Rothery DA (1987) Using the Landsat Thematic Mapper to detect and monitor active volcanoes: an example from Lascar volcano, northern Chile. *Geology* 15(7):614–617
- Ganci G, Vicari A, Cappello A, Del Negro C (2012) An emergent strategy for volcano hazard assessment: from thermal satellite monitoring to lava flow modeling. *Remote Sens Environ* 119:197–207. <https://doi.org/10.1016/j.rse.2011.12.021>
- Ganci G, James MR, Calvari S, Del Negro C (2013) Separating the thermal fingerprints of lava flows and simultaneous lava fountaining using ground-based thermal camera and SEVIRI measurements. *Geophys Res Lett* 40:5058–5063. <https://doi.org/10.1002/grl.50983>
- Ganci G, Cappello A, Bilotta G, Herault A, Zago V, Del Negro C (2018) Mapping volcanic deposits of the 2011–2015 Etna eruptive events using satellite remote sensing. *Front Earth Sci* 6:83. <https://doi.org/10.3389/feart.2018.00083>
- Ganci G, Cappello A, Zago V, Bilotta G, Herault A, Del Negro C (2019) 3D lava flow mapping of the 17–25 May 2016 Etna eruption using tri-stereo optical satellite data. *Ann Geophys* 62(2):VO220-VO220. <https://doi.org/10.4401/ag-7875>
- Ganci G, Cappello A, Bilotta G, Del Negro C (2020) How the variety of satellite remote sensing data over volcanoes can assist hazard monitoring efforts: the 2011 eruption of Nabro volcano. *Remote Sens Environ* 236:111426. <https://doi.org/10.1016/j.rse.2019.111426>
- Ganci G, Cappello A, Neri M (2022) Data fusion for satellite-derived earth surface: the 2021 topographic map of Etna Volcano. *Remote Sens* 15(1):198. <https://doi.org/10.3390/rs15010198>
- Ganci G, Bilotta G, Zuccarello F, Calvari S, Cappello A (2023) A multi-sensor satellite approach to characterize the volcanic deposits emitted during Etna's lava fountaining: the 2020–2022 study case. *Remote Sens* 15(4):916. <https://doi.org/10.3390/rs15040916>
- Gomez C, Setiawan MA, Listyaningrum N, Wibowo SB, Hadmoko DS, Suryanto W, Darmawan H, Bradak B, Daikai R, Sunardi S, Prasetyo Y, Astari AJ, Lukman L, Nurani IW, Dede M, Suhendro I, Lavigne F, Malawani MN (2022) LiDAR and UAV SfM-MVS of Merapi volcanic dome and crater rim change from 2012 to 2014. *Remote Sens* 14(20):5193. <https://doi.org/10.3390/rs14205193>
- Gouhier M, Pinel V, Belart JMC et al (2022) CNES-ESA satellite contribution to the operational monitoring of volcanic activity: the 2021 Icelandic eruption of Mt. Fagradalsfjall. *J Appl Volcanol* 11:10. <https://doi.org/10.1186/s13617-022-00120-3>
- Gray DM, Burton-Johnson A, Fretwell PT (2019) Evidence for a lava lake on Mt. Michael volcano, Saunders Island (South Sandwich Islands) from Landsat, Sentinel-2 and ASTER satellite imagery. *J Volcanol Geotherm Res* 379:60–71. <https://doi.org/10.1016/j.jvolgeores.2019.05.002>
- Harris AJ, Keszthelyi L, Flynn LP, Mougini-Mark PJ, Thornber C, Kauahikaua J, Sherrod D, Trusdell F, Sawyer MW, Flament P (1997) Chronology of the episode 54 eruption at Kilauea Volcano, Hawaii, from GOES-9 satellite data. *Geophys Res Lett* 24(24):3281–3284. <https://doi.org/10.1029/97GL03165>
- Harris AJ, Flynn LP, Rothery DA, Oppenheimer C, Sherman SB (1999) Mass flux measurements at active lava lakes: implications for magma recycling. *J Geophys Res* 104(B4):7117–7136. <https://doi.org/10.1029/98JB02731>
- Harris AJ, Flynn LP, Dean K, Pilger E, Wooster M, Okubo C, Mougini-Mark P, Garbeil H, De la Cruz-Reyna S, Rothery D, Wright R (2000) Real-time satellite monitoring of volcanic hot spots. Washington DC Am Geophys Union Geophys Monogr Ser 116:139–159
- Harris AJL, Pilger E, Flynn LP, Garbeil H, Mougini-Mark PJ, Kauahikaua J, Thornber C (2001) Automated, high temporal resolution, thermal analysis of Kilauea volcano, Hawai'i, using GOES satellite data. *Int J Remote Sens* 22(6):945–967. <https://doi.org/10.1080/014311601300074487>
- Harris AJ, Dehn J, James MR, Hamilton C, Herd R, Lodato L, Stefke A (2007) Pahoehoe flow cooling, discharge, and coverage

- rates from thermal image chronometry. *Geophys Res Lett* 34(19). <https://doi.org/10.1029/2007GL030791>
- Honda K, Nagai M (2002) Real-time volcano activity mapping using ground-based digital imagery. *ISPRS J Photogramm Remote Sens* 57:159–168. [https://doi.org/10.1016/S0924-2716\(02\)00112-0](https://doi.org/10.1016/S0924-2716(02)00112-0)
- James MR, Robson S, Pinkerton H, Ball M (2006) Oblique photogrammetry with visible and thermal images of active lava flows. *Bull Volcanol* 69:105–108
- James MR, Pinkerton H, Robson S (2007) Image-based measurement of flux variation in distal regions of active lava flows. *Geochem Geophys Geosyst* 8:Q03006. <https://doi.org/10.1029/2006G001448>
- James MR, Applegarth LJ, Pinkerton H (2012) Lava channel roofing, overflows, breaches and switching: insights from the 2008–2009 eruption of Mt. Etna *Bull Volcanol* 74:107–117
- James MR, Robson H (2014) Sequential digital elevation models of active lava flows from ground-based stereo time-lapse imagery. *ISPRS J Photogramm Remote Sens* 97:160–170. <https://doi.org/10.1016/j.isprsjprs.2014.08.011>
- James MR, Robson S, Smith MW (2017) 3-D uncertainty-based topographic change detection with structure-from-motion photogrammetry: precision maps for ground control and directly georeferenced surveys. *Earth Surf Process Landf* 42:1769–1788. <https://doi.org/10.1002/esp.4125>
- James MR, Carr B, D'Arcy F, Diefenbach A, Dietterich H, Fornaciai A, Lev E, Liu E, Pieri D, Rodgers M, Smets B, Terada A, von Aulock FW, Walter TR, Wood KT, Zorn EU et al (2020) Volcanological applications of unoccupied aircraft systems (UAS): Developments, strategies, and future challenges. *Volcanica* 3:67–114. <https://doi.org/10.30909/vol.03.01.67114>
- Jozkow G, Toth C, Grejner-Brzezinska D (2016) UAS topographic mapping with Velodyne LiDAR sensor. *ISPRS Annals Photogr, Remote Sens Spatial Inform Sci* III-1:201–208
- Lachlan-Cope T, Smellie JL, Ladkin R (2001) Discovery of a recurrent lava lake on Saunders Island (South Sandwich Islands) using AVHRR imagery. *J Volcanol Geotherm Res* 112(1-4):105–116. [https://doi.org/10.1016/S0377-0273\(01\)00237-2](https://doi.org/10.1016/S0377-0273(01)00237-2)
- Lague D, Brodu N, Leroux J (2013) Accurate 3D comparison of complex topography with terrestrial laser scanner: application to the Rangitikei canyon (N-Z). *ISPRS J Photogramm Remote Sens* 82:10–26. <https://doi.org/10.1016/j.isprsjprs.2013.04.009>
- Lormand C, Harris AJ, Chevrel MO, Calvari S, Gurioli L, Favalli M, Fornaciai L, Nannipieri L (2020) The 1974 west flank eruption of Mount Etna: a data-driven model for a low elevation effusive event. *Front Earth Sci* 8:590411. <https://doi.org/10.3389/feart.2020.590411>
- Marchese F, Filizzola C, Lacava T, Falconieri A, Faruolo M, Genzano N, Mazzeo G, Pietrapertosa C, Pergola N, Tramutoli V, Neri M (2021) Mt. Etna paroxysms of February–April 2021 monitored and quantified through a multi-platform satellite observing system. *Remote Sens* 13(16):3074. <https://doi.org/10.3390/rs13163074>
- Marsella M, Proietti C, Sonnessa A, Coltelli M, Tommasi P, Bernardo E (2009) The evolution of the Sciara del Fuoco subaerial slope during the 2007 Stromboli eruption: relation between deformation processes and effusive activity. *J Volcanol Geotherm Res* 182:201–213. <https://doi.org/10.1016/j.jvolgeores.2009.02.002>
- Marsella M, Nardinocchi C, Proietti C, Daga L, Coltelli M (2014) Monitoring active volcanoes using aerial images and the Orthoview tool. *Remote Sens* 6(12):12166–12186. <https://doi.org/10.3390/rs9030192>
- McGuire WJ (1996) Volcano instability: a review of contemporary themes. *Geol Soc Lond Spec Publ* 110(1):1–23. <https://doi.org/10.1144/GSL.SP.1996.110.01.01>
- Musacchio M, Silvestri M, Rabuffi F, Buongiorno MF, Falcone S (2023) Kilauea–Leilani 2018 lava flow delineation using Sentinel2 and Landsat8 images. *Geol Soc Lond, Spec Publ* 519(1):SP519–2020. <https://doi.org/10.1144/SP519-2020-118>
- Neal CA, Brantley SR, Antolik L, Babb JL, Burgess M, Calles K et al (2019) The 2018 rift eruption and summit collapse of Kilauea Volcano. *Science* 363(6425):367–374. <https://doi.org/10.1126/science.aav7046>
- Németh K, Martin U (2007) Practical volcanology, vol 207. Occasional Papers of the Geological Institute of Hungary
- Neri M, De Maio M, Crepaldi S, Suozzi E, Lavy M, Marchionatti F, Calvari S, Buongiorno MF (2017) Topographic maps of Mount Etna's summit craters, updated to December 2015. *J Maps* 13(2):674–683. <https://doi.org/10.1080/17445647.2017.1352041>
- Norini G, De Beni E, Andronico D, Polacci M, Burton M, Zucca F (2009) The 16 November 2006 flank collapse of the south-east crater at Mount Etna, Italy: study of the deposit and hazard assessment. *J Geophys Res Solid Earth* 114(B2). <https://doi.org/10.1029/2008JB005779>
- Oppenheimer C, Francis PW, Rothery DA, Carlton RW, Glaze LS (1993) Infrared image analysis of volcanic thermal features: Lascar Volcano, Chile, 1984–1992. *J Geophys Res Solid Earth* 98(B3):4269–4286. <https://doi.org/10.1029/92JB02134>
- Osman S, Rossi E, Bonadonna C, Frischknecht C, Andronico D, Cioni R, Scollo S (2019) Exposure-based risk assessment and emergency management associated with the fallout of large clasts at Mount Etna *Nat. Hazards Earth Syst Sci* 19:589–610. <https://doi.org/10.5194/nhess-19-589-2019>
- Patrick MR, Smellie JL, Harris AJL et al (2005) First recorded eruption of Mount Belinda volcano (Montagu Island), South Sandwich Islands. *Bull Volcanol* 67:415–422. <https://doi.org/10.1007/s00445-004-0382-6>
- Pedersen GBM, Pfeffer MA, Barsotti S, Tarquini S, de Michieli Vitturi M, Óladóttir B, Þrasstarson RH (2022) Lava flow hazard modelling during the 2021 Fagradalsfjall eruption, Iceland: applications of MrLavaLoba. *Nat Hazards Earth Syst Sci Discuss*. <https://doi.org/10.5194/nhess-2022-166>
- Pieri D, Abrams M (2004) ASTER watches the world's volcanoes: a new paradigm for volcanological observations from orbit. *J Volcanol Geotherm Res* 135(1-2):13–28. <https://doi.org/10.1016/j.jvolgeores.2003.12.018>
- Pinel V, Putra R, Solikhin A, Beauducel F, Santoso AB, Humaida H (2020) Tracking the evolution of the Merapi volcano crater area by high-resolution satellite. *Geophysical Research Abstracts* 22, EGU2020–5415, 2020, EGU General Assembly 2020.
- Pioli L, Palmas M, Behncke B, De Beni E, Cantarero M, Scollo S (2022) Quantifying Strombolian activity at Etna Volcano. *Geosciences* 12:163. <https://doi.org/10.3390/geosciences12040163>
- Proietti C, De Beni E, Coltelli M, Branca S (2011) The flank eruption history of Etna (1610–2006) as a constraint on lava flow hazard. *Ann Geophys* 54(5). <https://doi.org/10.4401/ag-5333>
- Proietti C, Coltelli M, Marsella M, Martino M, Scifoni S, Giannone F (2020) Towards a satellite-based approach to measure eruptive volumes at Mt Etna using Pleiades datasets. *Bull Volcanol* 82:35. <https://doi.org/10.1007/s00445-020-01374-8>
- Pyle DM, Mather TA, Biggs J (2013) Remote sensing of volcanoes and volcanic processes: integrating observation and modelling—introduction. *Geol Soc Lond, Spec Publ* 380(1):1–13. <https://doi.org/10.1144/SP380.14>
- Román A, Tovar-Sánchez A, Roque-Atienza D, Huertas IE, Caballero I, Fraile-Nuez E, Navarro G (2022) Unmanned aerial vehicles (UAVs) as a tool for hazard assessment: The 2021 eruption of Cumbre Vieja volcano, La Palma Island (Spain). *Sci Total Environ* 843. <https://doi.org/10.1016/j.scitotenv.2022.157092>

- Rupnik E, Daakir M, Pierrot Deseilligny M (2017) MicMac—a free, open-source solution for photogrammetry. *Open Geospatial Data, Software and Standards* 2(1):1–9. <https://doi.org/10.1186/s40965-017-0027-2>
- Spanu A, de Michieli Vitturi M, Barsotti S (2016) Reconstructing eruptive source parameters from tephra deposit: a numerical study of medium-sized explosive eruptions at Etna volcano. *Bull Volcanol* 78:59. <https://doi.org/10.1007/s00445-016-1051-2>
- Stevens NF, Wadge G, Murray JB (1999) Lava flow volume and morphology from digitised contour maps: a case study at Mount Etna, Sicily. *Geomorphology* 28:251–261. [https://doi.org/10.1016/S0169-555X\(98\)00115-9](https://doi.org/10.1016/S0169-555X(98)00115-9)
- Tanguy JC, Patanè G (1984) Activity of Mount Etna, 1977–1983: volcanic phenomena and accompanying seismic tremor. *Bull Volcanol* 47–4:965–976
- Thiele ST, Varley N, James MR (2017) Thermal photogrammetric imaging: a new technique for monitoring dome eruptions. *J Volcanol Geotherm Res* 337:140–145. <https://doi.org/10.1016/j.jvolgeores.2017.03.022>
- Torres R, Mouginiis-Mark P, Self S, Garbeil H, Kallianpur K, Quiambao R (2004) Monitoring the evolution of the Pasig–Potrero alluvial fan, Pinatubo Volcano, using a decade of remote sensing data. *J Volcanol Geotherm Res* 138(3–4):371–392. <https://doi.org/10.1016/j.jvolgeores.2004.08.005>
- Turner NR, Perroy RL, Hon K (2017) Lava flow hazard prediction and monitoring with UAS: a case study from the 2014–2015 Pāhoā lava flow crisis. *Hawai'i J Appl Volcanol* 6:17. <https://doi.org/10.1186/s13617-017-0068-3>
- Vicari A, Ganci G, Behncke B, Cappello A, Neri M, Del Negro C (2011) Near-real-time forecasting of lava flow hazards during the 12–13 January 2011 Etna eruption. *Geophys Res Lett* 38(13):1–7. <https://doi.org/10.1029/2011GL047545>
- Wadge G, Guest JE (1981) Steady-state magma discharge at Etna 1971–1981. *Nature* 294:548–550. <https://doi.org/10.1038/294548a0>
- Wakeford ZE, Chmielewska M, Hole MJ, Howell JA, Jerram DA (2019) Combining thermal imaging with photogrammetry of an active volcano using UAV: an example from Stromboli Italy. *The Photogrammetric Record* 34(168):445–466. <https://doi.org/10.1111/phor.12301>
- Walker GPL (1971) Compound and simple lava flows and flood basalts. *Bull Volcanol* 35(3):579–590. <https://doi.org/10.1007/BF02596829>
- Walker GPL (1973) Lengths of lava flows. *Philosophical Transactions of the Royal Society of London. Series A, Mathematic Phys Sci* 274(1238):107–118. <https://doi.org/10.1098/rsta.1973.0030>
- Wood CA (1980) Morphometric evolution of cinder cones. *J Geophys Res* 7(3–4):387–413. [https://doi.org/10.1016/0377-0273\(80\)90040-2](https://doi.org/10.1016/0377-0273(80)90040-2)
- Wooster MJ, Rothery DA (1997) Thermal monitoring of Lascar Volcano, Chile, using infrared data from the along-track scanning radiometer: a 1992–1995 time series. *Compound and simple lava flows and flood basalts. Bull Volcanol* 58:566–579

Listing of used software

- <https://www.ct.ingv.it/index.php/monitoraggio-e-sorveglianza/segna-li-in-tempo-reale/video-sorveglianza-vulcanica-etna> accessed on 29 March 2023
- <https://www.agisoft.com>. Accessed 01 September 2022
- <https://www.blumarblegeo.com/global-mapper/>. Accessed 18 November 2022
- <https://www.danielgm.net/cc/>. Accessed 01 September 2022
- <https://desktop.arcgis.com/en/arcmap/10.6/tools/spatial-analyst-toolbox/kernel-density.htm>. Accessed 01 September 2022
- <https://www.esri.com/en-us/arcgis/about-arcgis/overview>. Accessed 01 September 2022
- <http://ring.gm.ingv.it/>. Accessed 01 September 2022